Université du Québec
Institut National de la Recherche Scientifique
Centre Énergie Matériaux Télécommunications

Development of Broadband Nanostructured Photocatalysts for Environmental Remediation

Par

Guolong Song

Mémoire présentée pour l'obtention du grade de
Maître ès sciences (M.Sc.)
en sciences de l'énergie et des matériaux

Jury d'évaluation

Président du jury et examinateur interne	Prof. Mohamed Mohamedi INRS-ÉMT, Université du Québec
Examinateur externe	Prof. Nianqiang Wu Department of Chemical Engineering University of Massachusetts Amherst
Examinateur interne	Prof. Mohamed Mohamedi INRS-ÉMT, Université du Québec
Directeur de recherche	Prof. Dongling Ma INRS-ÉMT, Université du Québec
Codirecteur de recherche	Prof. Zhi Chen Concordia University

REMERCIEMENTS

Foremost, I would like to thank my supervisor, Prof. Dongling Ma for the continuous support of my Master's study and research activities. She has created a warm and free research environment allowing me to explore my interest in the forefront and fascinating scientific field. Without whom, I could not have made it possible. Being able to study under her supervision is one of the most important achievements in my life.

I would like also to express my sincere gratitude to Dr. Qingzhe Zhang, Dr. Fan Yang and Dr. Xiaolei Liu. They have made vital contributions to most of my work and given me invaluable help and comments on my research and thesis writing.

I would like to also thank all group members, Shengyun Huang, Yong Wang, Ting Yu, Wanting He, and Chen Wang, for their help throughout the duration of my master's study.

I am grateful to all my friends who have made the last two years so enjoyable.

Finally, I thank the departmental and technical staff at INRS-EMT.

RÉSUMÉ

Un photocatalyseur à large bande de l'hétérojonction de type II des nanoforêts de TiO_2 (NFt) et du $ZnIn_2S_4$ en phase mixte est conçu et synthétisé pour la dégradation photocatalytique des MO. L'utilisation de la synthèse en une étape de $ZnIn_2S_4$ à phases mixtes en présence de TiO_2 NFt permet d'obtenir une efficacité de couplage élevée entre $ZnIn_2S_4$ et TiO_2 NFt. Les NFts $ZnIn_2S_4$-TiO_2 présentent une durabilité remarquable et une photoréponse étendue des régions ultraviolettes (UV) aux régions visibles, tout en présentant des performances photocatalytiques considérablement améliorées dans la dégradation du méthylorange (MO), quelle que soit l'exposition à la lumière solaire ou visible. Sous > 420 nm d'irradiation lumineuse, la constante de vitesse normalisée en masse des NFts $ZnIn_2S_4$-TiO_2 (0,00129 min^{-1} mg^{-1}) dépasse de loin celle du $ZnIn_2S_4$ (0,00098 min^{-1} mg^{-1}) de 1,3 fois. Pendant ce temps, il est augmenté à 2,5 fois sous irradiation solaire. Les mécanismes de la photodégradation sont découverts, en identifiant les intermédiaires actifs en réalisant des expériences de piégeage sous éclairage visible. Ce travail met en évidence le grand potentiel de développement de photocatalyseurs à large bande $ZnIn_2S_4$-TiO_2 NFt hautement efficaces pour faire face aux défis posés par la pollution de l'environnement.

Mots clés: TiO_2, $ZnIn_2S_4$, Photocatalyse, Hétérojonction, Dégradation du méthylorange

ABSTRACT

A broadband photocatalyst of the type-II heterojunction of TiO_2 nanoforests (NFts) and mixed-phase $ZnIn_2S_4$ is designed and synthesized for photocatalytic MO degradation. Utilizing one-step synthesis of mixed-phased $ZnIn_2S_4$ in the presence of TiO_2 NFts achieves the high coupling efficiency between $ZnIn_2S_4$ and TiO_2 NFts. The $ZnIn_2S_4$-TiO_2 NFts exhibits remarkable durability and wide photoresponse from the ultraviolet (UV) to visible regions, while it presents a tremendously enhanced photocatalytic performance in the degradation of methyl orange (MO) regardless of exposure to solar or visible light. Under $\lambda > 420$ nm light irradiation, the mass-normalized rate constant of the $ZnIn_2S_4$-TiO_2 NFts (0.00129 min^{-1} mg^{-1}) far exceeds that of the $ZnIn_2S_4$ (0.00098 min^{-1} mg^{-1}) by 1.3 times. Meanwhile, it is increased to 2.5 times under solar irradiation. The mechanisms of the photodegradation are uncovered, identifying the active intermediates by performing trapping experiments under visible light illumination. This work highlights the great potential of developing highly efficient $ZnIn_2S_4$-TiO_2 NFt broadband photocatalysts for coping with the challenges brought by environmental pollution

Keywords: TiO_2, $ZnIn_2S_4$, Photocatalysis, Heterojunction, MO Degradation.

SOMMAIRE RÉCAPITULATIF

DÉVELOPPEMENT DE PHOTOCATALYSEURS NANOSTRUCTURÉS À LARGE ABSORPTION DE LUMIÈRE POUR LA RESTAURATION DE L'ENVIRONNEMENT

0.1 Présentation

De nos jours, avec le développement rapide de l'industrialisation sociale et la croissance démographique dans la société moderne, un grand nombre de polluants nocifs et toxiques sont rejetés dans l'environnement écologique qui nous entoure [1-3]. Par conséquent, la pollution environnementale grave et la demande croissante d'énergie sont devenues deux problèmes mondiaux majeurs à l'ère actuelle. Heureusement, de plus en plus d'attention est portée à l'exploration de technologies vertes et respectueuses de l'environnement pour assurer le développement durable et sain de toute l'humanité. Parmi les technologies actuelles, la photocatalyse à base de semi-conducteurs est considérée comme l'une des technologies propres les plus prometteuses pour faire face à la pollution de l'environnement mondial [4,5]. La technologie de photocatalyse à semi-conducteurs peut réparer l'environnement par dégradation photocatalytique de divers polluants nocifs et toxiques [6-10].

Au cours des deux dernières décennies, d'énormes efforts ont été consacrés à la conception intelligente de matériaux nanostructurés pour la photocatalyse [11-23]. Parmi les divers photocatalyseurs prometteurs, le dioxyde de titane (TiO_2) est préféré et a été plus largement développé que tous les autres matériaux rapportés en raison de ses propriétés favorables uniques et diverses, notamment (i) permettant la manipulation de sa morphologie, (ii) fort Ti-O liaisons chimiques pour une excellente stabilité à long terme et une résistance à la photo-corrosion, (iii) une faible toxicité et une nature respectueuse de l'environnement, (iv) une disponibilité facile grâce à l'abondance des précurseurs, (v) une bande interdite avec 3,0-3,2 eV et une oxydation élevée.

Cependant, la large bande interdite (3,2 eV) empêche le TiO_2 de répondre aux exigences des applications pratiques car il ne peut répondre qu'à la lumière ultraviolette ou proche ultraviolette, ce qui se traduit par une faible efficacité d'utilisation de l'énergie solaire [25]. Par conséquent, afin de mieux utiliser l'énergie solaire, le développement de photocatalyseurs d'irradiation à la lumière visible a attiré une large attention. Jusqu'à présent, les chercheurs ont développé ou inventé divers photocatalyseurs irradiés par la lumière visible, tels que TiO_2, oxyde simple Fe_2O_3 [26], oxyde composite Ag_3PO_4 [27], Bi_2MoO_6 [28] et Bi_2WO_6 [29], chalcogénure métallique CdS [30] et bientôt. Parmi ces catalyseurs sensibles à la lumière visible, les composés de soufre métallique ont été largement étudiés en raison de leurs propriétés photoélectrocatalytiques uniques et de leur stabilité chimique relative. De plus, de nouveaux chalcogénures métalliques ternaires ont attiré une large attention ces dernières années [31].

Le sulfure de zinc et d'indium ($ZnIn_2S_4$) est un sulfure de métal ternaire typique avec d'excellentes performances photocatalytiques. Il a une structure en couches et peut présenter trois formes cristallines différentes, y compris la phase cubique, la phase hexagonale et la phase rhomboïde. Chaque forme cristalline de $ZnIn_2S_4$ présente des performances photocatalytiques sous irradiation à la lumière visible. Sur la base de la structure en couches, les chercheurs ont réussi à synthétiser des micro / nano structures $ZnIn_2S_4$ avec différentes caractéristiques morphologiques. $ZnIn_2S_4$ a une largeur de bande interdite appropriée. Il y a une réponse positive dans la région de la lumière visible [32-35]. Dans le même temps, comparé aux sulfures métalliques traditionnels tels que le CdS [30] et le Sb_2S_3 [36], le $ZnIn_2S_4$ est moins toxique et présente des propriétés optiques similaires, ce qui montre qu'il a une large gamme d'applications dans la protection de l'environnement et d'autres chalcogénures métalliques ternaires comme $CuGaS_2$ [37] et comparé au $ZnIn_2S_4$ [38], $ZnIn_2S_4$ a une large gamme de sources, une composition chimique simple, une préparation relativement facile et montre une stabilité chimique considérable dans le processus photocatalytique [39]. Par conséquent, $ZnIn_2S_4$ a attiré une large attention en raison de ses propriétés physiques et chimiques attrayantes, ainsi que de son faible coût, de sa faible toxicité et de sa préparation facile. Sur la base des avantages ci-dessus, $ZnIn_2S_4$ a de larges perspectives d'application dans les domaines du dégagement d'hydrogène, de la réduction du CO_2, de la synthèse organique sélective et de la protection de l'environnement sous lumière visible.

Cette thèse se concentre sur la recombinaison supprimée des électrons et des trous photogénérés, pour $ZnIn_2S_4$ dans les familles hexagonales, en utilisant l'effet positif du TiO_2 hiérarchique, y compris le transfert d'électrons rapide, la longue durée de vie des électrons et le chemin optique prolongé, pour développer un photocatalyseur à large bande pour la remise en état de l'environnement.

Ce manuscrit est divisé en 3 chapitres distincts:

- Le premier chapitre détaillera la structure, les propriétés et la modification de TiO_2 et $ZnIn_2S_4$

- Le deuxième chapitre est consacré à tous les outils de préparation et de caractérisation du TiO_2.

- Le troisième chapitre présentera les résultats expérimentaux obtenus et analysera ses caractéristiques structurelles, ses propriétés optiques et ses performances photocatalytiques.

0.2 Structure, propriétés et modification du dioxyde de titane

0.2.1 Structure cristalline du TiO_2

TiO_2 existe 3 phases dans la nature: rutile (tétragonale), anatase (tétragonale) et brookite (orthorhombique), où il existe 2 phases les plus courantes d'anatase et de rutile en raison de la brookite possédant une faible symétrie cristallographique et une faible stabilité thermique. Toutes ces phases peuvent être décrites comme un arrangement d'octaèdres TiO_6 légèrement déformés, reliés par des sommets ou des crêtes, tandis que l'oxygène montre une triple coordination [11]. Ces 3 structures cristallines sont illustrées à la figure 0.1.

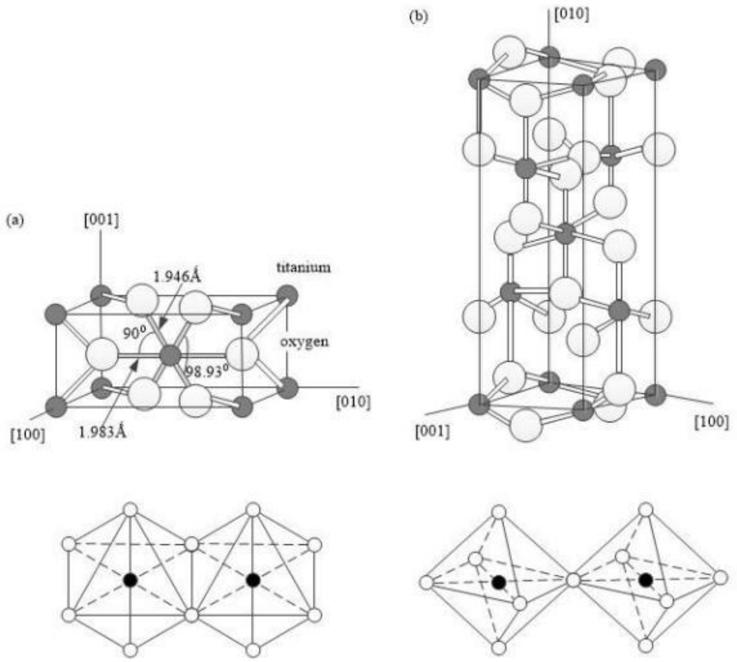

Figure 0.1 Structure cristalline de (a) rutile et (b) anatase.

Le rutile est plus dense (4,250 g / cm^3) que l'anatase (3,894 g / cm^3). Bien que la phase rutile soit la plus stable de toutes (à des pressions inférieures à 60 kPa), la différence d'énergie interne avec la phase anatase est faible, indiquant que la phase anatase est une phase métastable. Ainsi, la TiO_2 anatase peut être facilement obtenue par synthèse à basse température (inférieure à 400 ^{o}C), tandis que la phase rutile, selon les conditions de pression, commence à apparaître entre 400 et 600 ^{o}C, et devient la phase dominante à des températures supérieures à 600 ^{o}C.

Bien que la bande interdite de la phase rutile soit plus petite que celle de la phase anatase (comme le montre le tableau 0.1), l'efficacité photoélectrolytique est plus grande pour la phase anatase. Plusieurs explications existent à ce fait contre-intuitif: différence de taux de Fermi, mobilité des porteurs de charge, ou augmentation de la concentration de radical hydroxyle pour la phase anatase. Luttrell et coll. suggèrent que la différence est principalement due à la mobilité des porteurs de charge. Pendant ce temps, la bande interdite plus grande de l'anatase avec 3,2 eV fournit une capacité d'oxydation plus forte, ce qui permet d'obtenir une dégradation plus approfondie des polluants organiques.

Tableau 0.1 Données de structure cristalline pour TiO_2.

Phase	Rutile	Anatase	Brookite
Lattice system	Tetragonal	Ttetragonal	Orthorhombic
Lattice parameter	a=4.5936 Å c=2.9587 Å	a=3.784 Å c=9.515 Å	a=9.184 Å b=5.447 Å c=5.154 Å
Space group	P42/mnm	I41/amd	Pbca
Ti-O bond length	1.949(4) Å 1.908(2) Å	1.937(4) Å 1.965(2) Å	1.87-2.04 Å
O-Ti-O bond angle	81.2° 90.0°	77.7° 92.6°	77.0°-105°
Bandgap	3.02 eV	3.20 eV	2.96 eV

0.2.2 Structure de bande électronique de TiO_2

La structure de bande électronique des matériaux semi-conducteurs se compose généralement d'une bande de valence à basse énergie (VB) remplie d'électrons et d'une bande de conduction à haute énergie (CB) vide. La partie du bas de la bande de conduction au haut de la bande de valence est appelée la bande interdite (Eg), qui est numériquement égale à la différence de niveau d'énergie entre la bande de conduction et la bande de valence.

Le TiO_2 est un matériau semi-conducteur à large bande interdite. Les bandes interdites de l'anatase, de la brookite et du rutile sont respectivement de 3,20 eV, 2,96 eV et 3,02 eV.

Lorsque l'énergie photonique du matériau photocatalytique semi-conducteur TiO_2 est supérieure à la bande interdite, les électrons de la bande de valence sautent vers la bande de conduction lorsqu'ils sont excités, faisant de l'O^2- dans la bande de valence O^- et laissant les trous correspondants, Ti^{4+} dans le la bande de conduction devient des électrons photogénérés Ti^{3+}, formant ainsi des paires électron-trou. Les trous photo-générés ont une forte capacité d'oxydation, qui peut absorber et capturer des électrons à la surface des semi-conducteurs ou dans des solvants, les provoquant ainsi à s'oxyder; les électrons photo-générés ont une forte capacité de réduction, ce qui peut amener l'accepteur d'électrons sur la surface du semi-conducteur à accepter des électrons et à être réducteur. Les électrons et trous photo-générés forment un système redox.

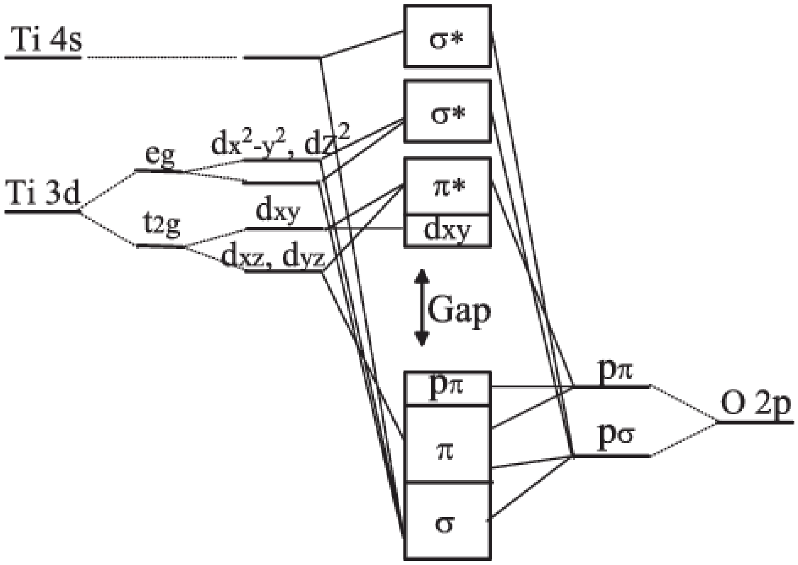

Figure 0.2 Structure de bande électronique de l'anatase.

TiO_2 est un semi-conducteur de type N. La figure 0.2 montre que la BV (bande de valence) est principalement dominée par l'orbitale 2p de l'atome O. L'orbitale 3d de l'atome de titane est au bas du BC (bande de conduction). Cette présence d'oxygène dans BV justifie le fait que TiO_2 est un semi-conducteur de type N car pour chaque oxygène manquant dans la structure, il y a 2 électrons libres compensés par les centres Ti^{3+}.

Pour la phase anatase, la bande interdite est de 3,2 eV, ce qui signifie que la TiO_2 anatase absorbe les photons de longueur d'onde inférieure ou égale à 380 nm. La TiO_2 anatase absorbe donc dans la région UV du spectre solaire, ce qui correspond à moins de 5% de l'énergie solaire.

0.2.3 Le mécanisme photocatalytique du TiO_2

Comme le montre la figure 0.3 [12-14], la lumière avec une énergie supérieure à la largeur de bande interdite de TiO_2 excitera les électrons (e^-), et les électrons photogénérés passeront de la bande de valence à la bande de conduction, laissant un vide dans le bande de valence. Trou (h^+), formant une paire électron-trou photo-générée. En raison de la discontinuité de la bande interdite de TiO_2, il peut empêcher la recombinaison d'électrons et de trous photo-générés, et faire subir aux électrons et aux trous des réactions d'oxydo-réduction avec les substances adsorbées en surface. Le processus de réaction total est indiqué dans le tableau ci-dessous.

0.3 Caractérisation structurale et morphologique

0.3.1 Caractérisation structurale et morphologique des NFt TiO_2

La figure 0.3 présente les résultats de la caractérisation structurale et morphologique des NFt TiO_2. À partir des images de SEM (Figure 0.3.a, b et c), les caractéristiques structurelles de TiO_2 NFts est que les nanofils de TiO_2 à haute densité sont développés vers l'extérieur à partir de l'ensemble du tronc TiO_2 primaire avec une longueur de 1-2 µm. En outre, on peut observer que l'échantillon a une morphologie uniforme. Dans les images de TEM (Figure 0.3d, e), les branches ultrafinies peuvent être observées plus clairement et l'espacement d mesuré de ~ 0,35, ~ 0,37 et ~ 0,38 nm peut être indexé sur l'espacement du réseau du plan (101) de l'anatase . Correspond à l'ensemble des anneaux de diffraction indexés à l'anatase dans le diagramme de diffraction d'électrons de zone sélectionnée (SAED) (Figure 0.3f), il est déterminé que le composant de TiO_2 NFts contient uniquement l'anatase, en bon accord avec ces résultats de la littérature [13-16].

Afin de déterminer davantage la composition et la pureté des catalyseurs préparés, l'échantillon de TiO_2 NFts a été caractérisé par XRD et XPS (figure 0.4). D'après la figure 0.4a, les pics de diffraction indexés sur la phase anatase du TiO_2 (JCPDS 21-1272) sont clairement observés pour TiO_2 NFts. Les résultats ci-dessus indiquent que le TiO_2 NFts est une anatase monophasique et présente une cristallinité élevée. La mesure XPS est effectuée pour étudier les états d'oxydation du Ti et de l'O dans ces échantillons. Comme le montre la figure 0.4b, les deux pics de Ti $2p_{3/2}$ et Ti $2p_{1/2}$ sont attribués aux composants Ti (IV), indiquant que le Ti (IV) est l'état d'oxydation dominant dans ces échantillons. Pour les spectres O 1s (figure 0.4c), il peut être équipé de trois pics. L'un est centré à ~ 530 eV, caractéristique de l'oxygène du réseau (noté Ti-O-Ti) et le second situé à ~ 532,7 eV est indexé sur l'oxygène de surface (noté Ti-OH), et le pic le plus faible est situé à ~ 527,8 eV, qui est acceptée comme espèce d'impureté de $C_2O_4^{2-}$ de PTO. De toute évidence, la surface du pic d'oxygène de surface dans le TiO2 NFts est plus forte que le P25 commercial, ce qui correspond aux caractéristiques structurelles des TiO_2 NFts, ce qui implique plus de sites tensioactifs fournis par ses branches, ce qui crée un environnement avantageux pour la transmission d'électrons et la séparation de charge. des NFts TiO_2 modifiés par $ZnIn_2S_4$.

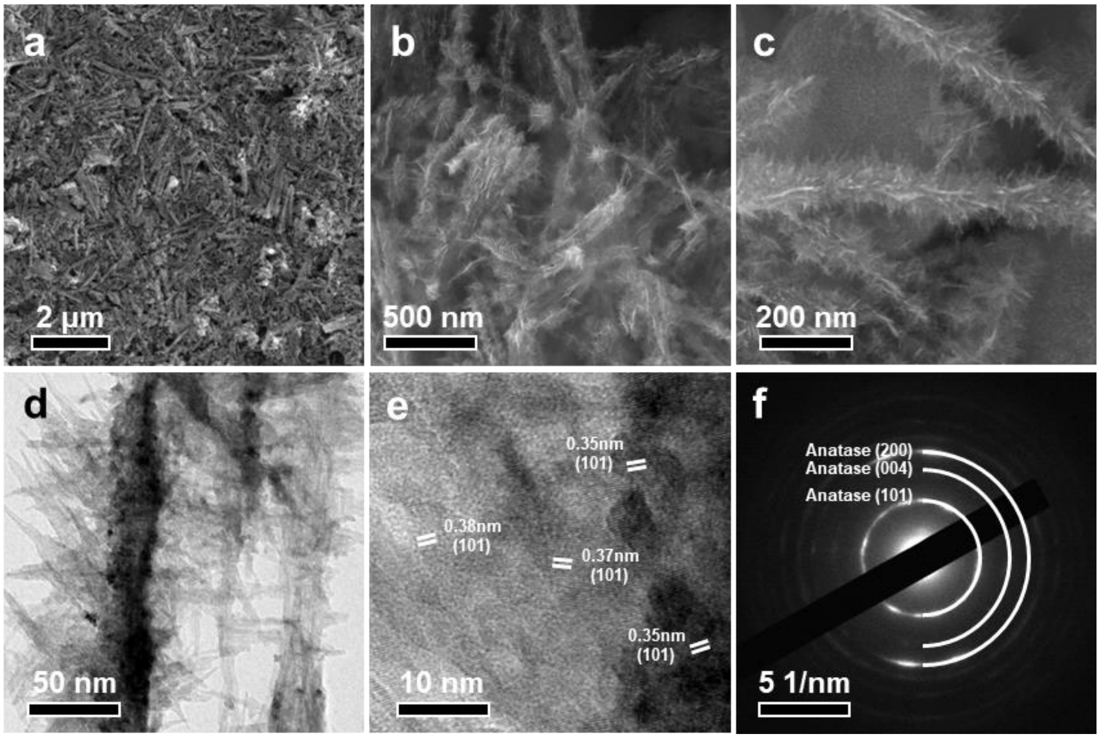

Figure 0.3 Images SEM (a-c), images TEM (d, e) et motif SAED (f) de TiO_2 NFts.

Les nanofils de TiO_2 ultrafinis offrent une surface spécifique élevée pour la fixation du $ZnIn_2S_4$ et la collecte de la lumière, un contact étroit pour la migration des porteurs et des sites plus actifs avec des polluants, tandis que les grands troncs centraux améliorent la diffusion de la lumière. Ces caractéristiques des NFts TiO_2 se traduisent par une extension considérable de la distance de propagation de la lumière au sein de l'ensemble des NFts TiO_2 et augmentent ainsi la probabilité d'absorption des photons des NFts TiO_2. La capacité photocatalytique pourrait être grandement favorisée par une telle interaction synergique des différentes parties de TiO_2 NFts. Ces avantages se reflètent dans les performances de dégradation grandement améliorées du photocatalyseur $ZnIn_2S_4$-TiO_2 NFts mentionné plus loin.

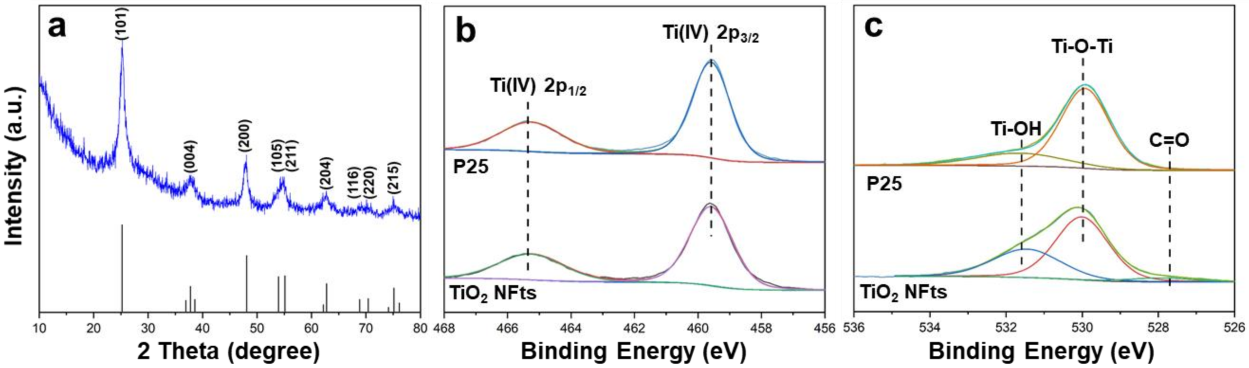

Figure 0.4 Modèles XRD (a) de TiO_2 NFts et spectres XPS de Ti 2p (b) et O 1s (c) de TiO_2 NFts et P25 commercial. L'encart dans a est le modèle de poudre XRD standard de l'anatase (JCPDS 21-1272).

0.3.2 Caractérisation structurale et morphologique des NFts $ZnIn_2S_4$-TiO_2 et des photocatalyseurs comparatifs

Les caractéristiques structurelles des $ZnIn_2S_4$-TiO_2 NFts et des photocatalyseurs comparatifs sont examinées par XRD (comme le montre la figure 0.5). Les pics de diffraction indexés sur la phase anatase du TiO_2 (JCPDS 21-1272) correspondaient aux caractéristiques cristallographiques des TiO_2 NFts, peuvent être observés dans les motifs des hybrides $ZnIn_2S_4$-TiO_2 NFts, et le mélange de $ZnIn_2S_4$ et TiO_2 NFts. Pour le $ZnIn_2S_4$, deux ensembles de pics proéminents sont exposés, où les pics à 14,4°, 27,8°, 33,7° et 48,4° attribués aux plans (111), (311), (400) et (440) du cube $ZnIn_2S_4$ (JCPDS 48-1778) et les pics à 21,6°, 27,7° et 30,4° correspondent aux plans hexagonaux (006), (102) et (104) $ZnIn_2S_4$ (JCPDS 65-2023), suggérant la formation de phase et coexistence de deux phases différentes dans les photocatalyseurs à base de $ZnIn_2S_4$, ce qui présente la possibilité de générer une homojonction par le $ZnIn_2S_4$ cubique et hexagonal. Il permettra aux TiO_2 NFts de se combiner avec le $ZnIn_2S_4$ hexagonal pour surmonter sa recombinaison de porteurs et améliorer encore les performances de photodégradation via la combinaison de TiO_2 NFts et d'homojonction $ZnIn_2S_4$.

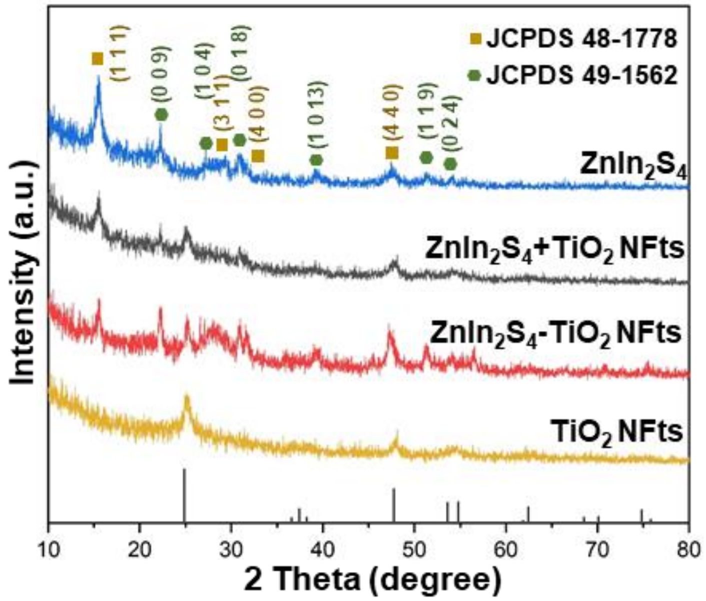

Figure 0.5 Modèles XRD de $ZnIn_2S_4$, TiO_2 NFt, hybride $ZnIn_2S_4$-TiO_2 NFt et mélange de photocatalyseurs $ZnIn_2S_4$ et TiO_2 NFt. L'encart est le modèle de poudre XRD standard d'anatase (JCPDS 21-1272).

La morphologie et la structure du photocatalyseur $ZnIn_2S_4$-TiO_2 NFt ont été minutieusement étudiées par diverses techniques (figure 0.6). Comme le montre la figure 3.4a-c, le $ZnIn_2S_4$ est composé avec le TiO_2 NFt et fait une distinction claire entre deux types de particules avec des morphologies individuelles, y compris des nanofeuilles minces et des nanocubes. Avec une exploration plus approfondie par des images MET à haute résolution (Figure 0.6d, e), l'espacement d mesuré ~ 0,31 nm, ~ 0,32 nm et ~ 0,33 nm peut être indexé sur l'espacement du réseau des plans (102) et (100) de le $ZnIn_2S_4$ hexagonal et ~0,38 nm peuvent être indexés à celui du $ZnIn_2S_4$ cubique. Notamment, un ensemble d'angle caractéristique de (100) plans de réseaux hexagonaux peut être observé, ce qui illustre davantage l'existence de ZnIn2S4 hexagonal. Pendant ce temps, le modèle SAED de $ZnIn_2S_4$-TiO_2 NFts présente clairement trois ensembles d'anneaux de diffraction correspondant à $ZnIn_2S_4$ cubique et $ZnIn_2S_4$ rhomboédrique et à l'anatase, respectivement. Ces résultats ont confirmé au préalable les trois composants contenus dans le photocatalyseur $ZnIn_2S_4$-TiO_2 NFts tel que synthétisé, en bon accord avec l'analyse des motifs XRD.

Pour étudier plus en détail la distribution élémentaire de Ti, O, Zn, In et S, des images de cartographie EDS sont présentées à la figure 0.6h-l, dans laquelle le Zn, In et S sont uniformément distribués dans les NFts $ZnIn_2S_4$-TiO_2. Pour la distribution du Ti et O, les contours de TiO_2 NFts sont encore discernables, qui se chevauchent dans la région de $ZnIn_2S_4$. Une telle distribution peut être facilement vu que le $ZnIn_2S_4$ est composé avec TiO_2 NFts pour construire une hétérojonction, ce qui peut faciliter la transmission des porteurs et l'utilisation de la lumière par tous les composants. En outre, cela indique que les NFts TiO_2 servent de support au $ZnIn_2S_4$, et qu'ils sont capables de conserver leurs caractéristiques cristallines initiales lors de l'introduction de ces composants. Le photocatalyseur $ZnIn_2S_4$-P25 était un échantillon comparatif pour les NFts $ZnIn_2S_4$-TiO_2.

La morphologie et la structure de $ZnIn_2S_4$-P25 ont été étudiées par TEM et SAED (figure 0.7). Comme le montrent les figures 0.7a et b, le $ZnIn_2S_4$ est également composé avec le P25. En outre, le modèle SAED de $ZnIn_2S_4$-TiO_2 NFts présente clairement trois ensembles d'anneaux de diffraction correspondant à $ZnIn_2S_4$ cubique et $ZnIn_2S_4$ rhomboédrique et à l'anatase, respectivement. Ces résultats ont confirmé au préalable les composants similaires dans le photocatalyseur $ZnIn_2S_4$-P25 tel que synthétisé avec des NFts $ZnIn_2S_4$-TiO_2. Pendant ce temps, il vérifie que le TiO_2 ne jouera pas le rôle provoquant des changements dans la structure cristalline et la morphologie pour la synthèse de $ZnIn_2S_4$.

Pour étudier plus en détail la distribution élémentaire de Ti, O, Zn, In et S, des images de cartographie EDS sont présentées à la figure 0.7d-i, dans laquelle le Zn, In et S sont uniformément répartis dans le $ZnIn_2S_4$-P25. Pour la distribution de Ti et O, P25 se chevauche dans la région de $ZnIn_2S_4$. Une telle distribution peut être facilement vu que le $ZnIn_2S_4$ est composé avec P25 pour construire une hétérojonction.

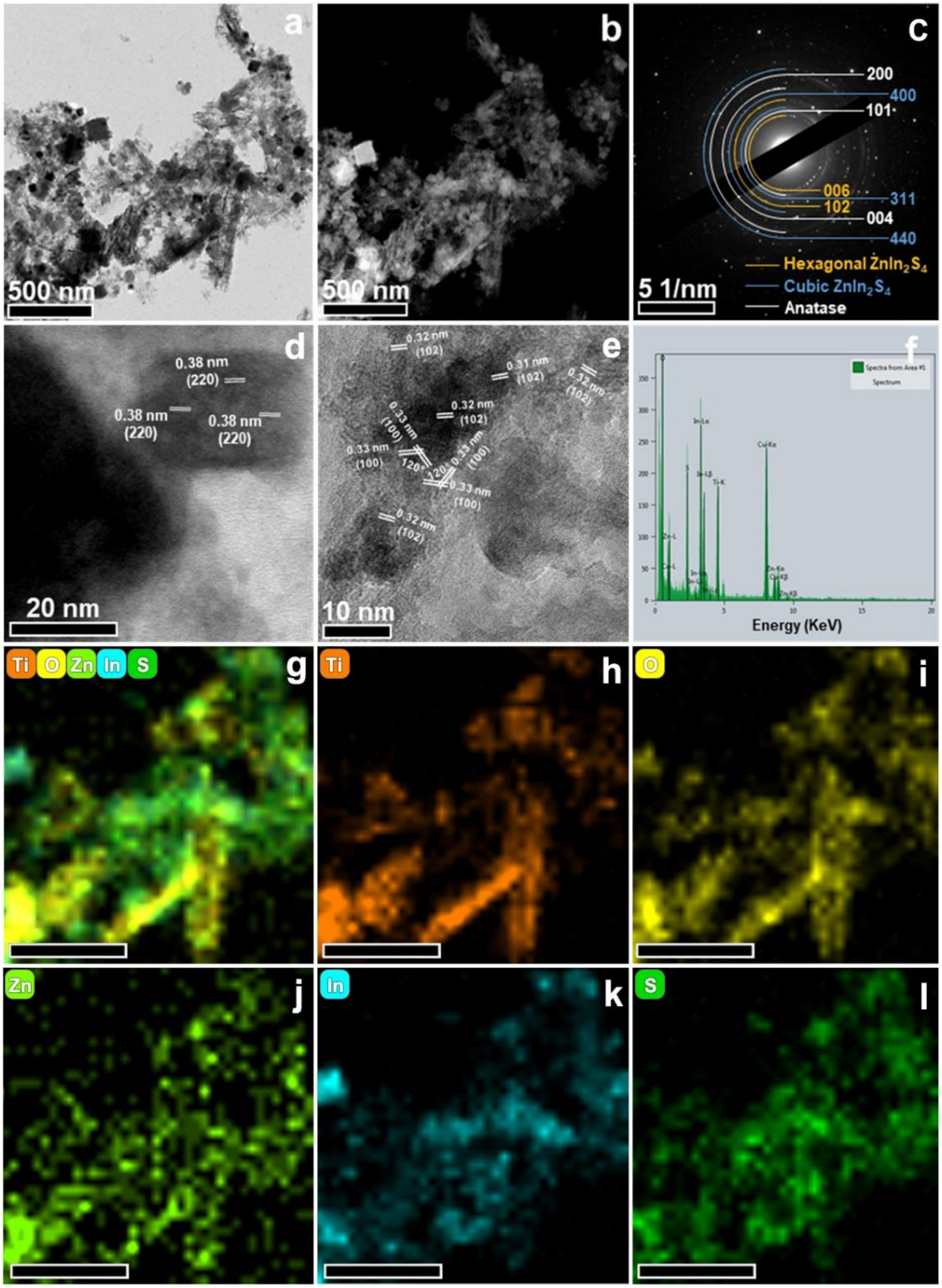

Figure 0.6 Images MET (a, b, d, e), motif SAED (c), spectres EDS (f) et cartographie élémentaire correspondante (g-l) des photocatalyseurs $ZnIn_2S_4$-TiO_2 NFt. Les barres en (g)-(l) correspondent aux 500 nm.

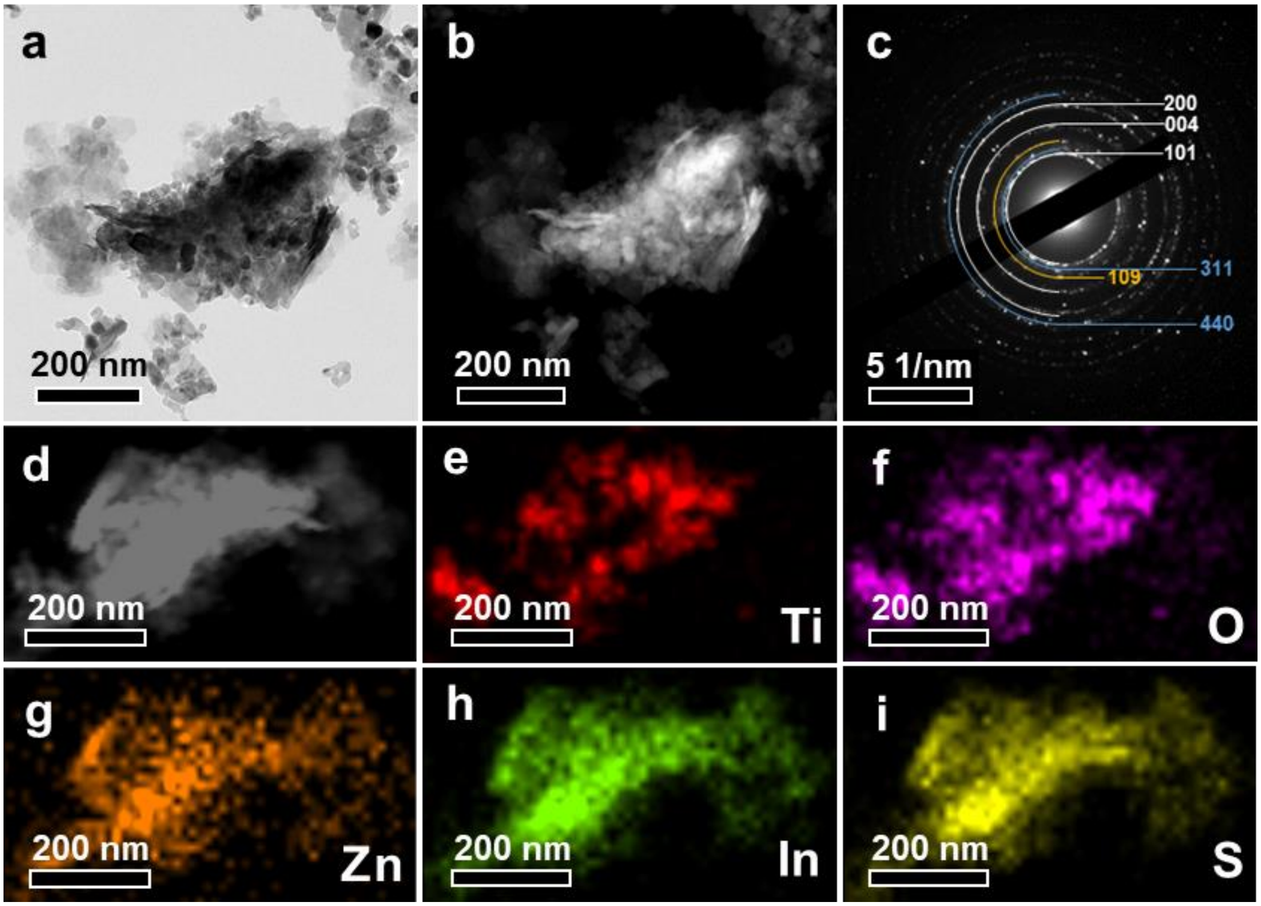

Figure 0.7 Images TEM (a, b et d), motif SAED (c) et cartographie élémentaire correspondante (d-i) du photocatalyseur $ZnIn_2S_4$-P25. Les anneaux de diffraction marqués en jaune, bleu et blanc en c correspondent respectivement au $ZnIn_2S_4$ rhomboédrique, au $ZnIn_2S_4$ cubique et à l'anatase.

0.3.3 Propriétés optiques

Pour la comparaison des propriétés optiques, les spectres d'absorption UV-vis des photocatalyseurs $ZnIn_2S_4$-TiO_2 NFts, $ZnIn_2S_4$-P25, TiO_2 NFts, $ZnIn_2S_4$ et P25 ont été enregistrés comme présenté dans la figure 3.6. Dans la région UV-vis, la caractéristique d'absorption typique de $ZnIn_2S_4$ rhomboédrique avec un bord d'absorption à ~ 500 nm est observée dans les échantillons impliquant $ZnIn_2S_4$. Elle correspond à l'excitation électronique de la bande de valence (VB) à la bande de conduction (CB) du $ZnIn_2S_4$ rhomboédrique qui représente une énergie de bande interdite de ~2,5 eV. Le TiO_2 NFts présente une absorption inférieure à 380 nm, correspondant aux propriétés optiques de l'anatase qui a fourni une bande interdite de ~ 3,2 eV et l'absorption optique invalide dans la région de λ > 420 nm.

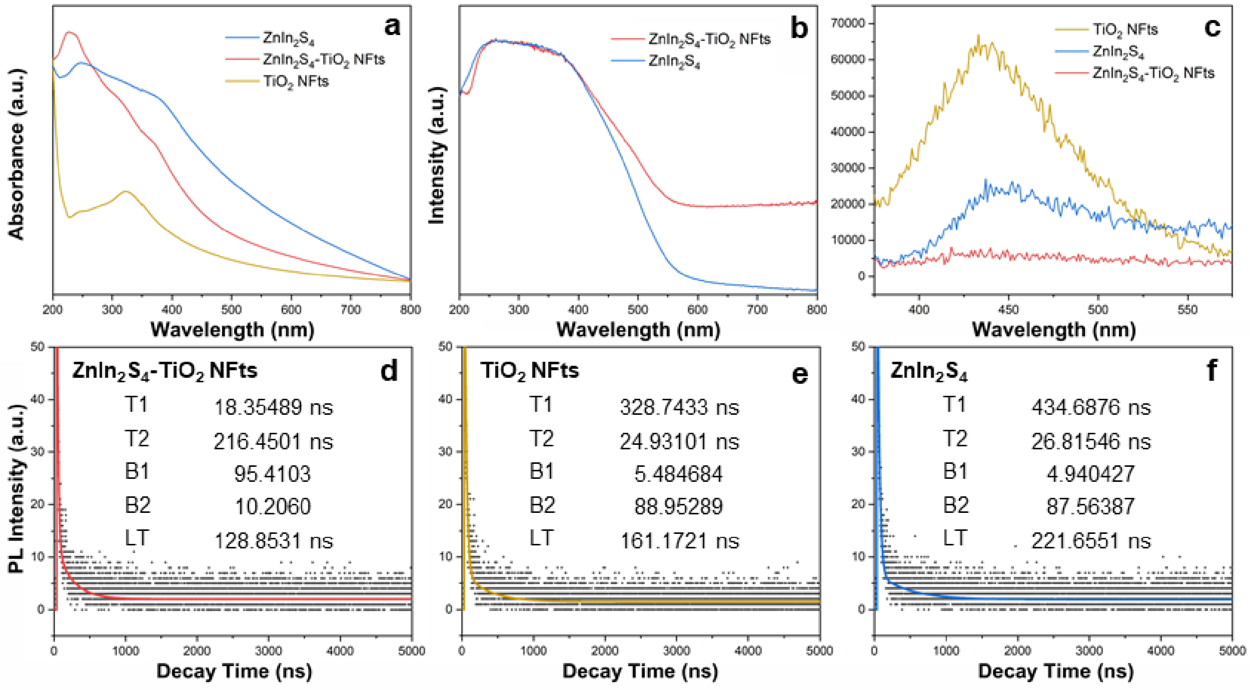

Figure 0.8 Spectres d'absorption UV-vis (a), spectres DRS (b), spectres PL à l'état d'équilibre (c) avec l'excitation à 375 nm et courbes de décroissance TRPL (df) mesurées à 440 nm des NFts $ZnIn_2S_4$-TiO_2, $ZnIn_2S_4$ et TiO_2 NFt.

La figure 3.6c montre les spectres de photoluminescence (PL) en régime permanent des échantillons $ZnIn_2S_4$-TiO_2, $ZnIn_2S_4$ et TiO_2. La trempe PL dans les $ZnIn_2S_4$-TiO_2 NFts indique une recombinaison fortement supprimée, ce qui peut être attribué au transfert efficace de charge interfaciale de $ZnIn_2S_4$ aux NFts TiO_2. La dynamique des porteurs de charge a été étudiée par spectroscopie PL à résolution temporelle (TRPL) (Figure 3.6d-f). Une équation d'ajustement biexponentiel a été appliquée pour analyser les courbes de décroissance TRPL en raison de leur complexité. La cinétique de désintégration des NFts $ZnIn_2S_4$-TiO_2 montre une durée de vie moyenne des PL plus courte (129 ± 5 ns) que celles de ZIS (222 ± 4 ns) et TNF (161 ± 2 ns). La durée de vie réduite du PL dans l'hétérojonction $ZnIn_2S_4$-TiO_2 NFts soutient que l'introduction du ZIS peut faciliter efficacement la séparation des porteurs de charge photogénérés.

0.4 Performance photocatalytique

La figure 0.9 illustre les taux de dégradation photocatalytique de MO à partir d'une solution aqueuse (25 mL de 30 mg / L MO) pour divers photocatalyseurs en fonction du temps sous éclairage visible ($\lambda >$ 420 nm). Sous lumière visible, tous les autres échantillons présentent une activité photocatalytique plus élevée que le photocatalyseur TiO_2 NFts (figure 0.9a, b). TiO_2 NFts ne présentent aucune activité, indiquant que TiO_2 NFts ne présente aucune absorption optique dans la région de $\lambda >$ 420 nm. C'est un résultat cohérent avec les résultats des spectres d'absorption UV-vis et de la littérature [13]. Tous les échantillons impliquant $ZnIn_2S_4$ présentent un taux de dégradation de MO plus élevé que celui des échantillons de TiO_2 pur. Par conséquent, le $ZnIn_2S_4$ semble favoriser davantage l'activité photocatalytique sous un éclairage en lumière visible. Pour le photocatalyseur de mélange de $ZnIn_2S_4$ et TiO_2 NFts (dénommé $ZnIn_2S_4$ + TiO_2 NFts), ses performances semblent être presque les mêmes que celles de $ZnIn_2S_4$, confirmant en outre que TiO_2 NFts ne présente aucune réponse à la lumière visible. La figure 3.8b montre l'étude cinétique de la dégradation de MO sur chaque photocatalyseur. La constante de vitesse calculée à partir du modèle de réaction du premier ordre suit l'ordre : $ZnIn_2S_4$-TiO_2 NFts> $ZnIn_2S_4$> $ZnIn_2S_4$-P25> $ZnIn_2S_4$ + P25> $ZnIn_2S_4$ + TiO_2 NFts> P25> TiO_2 NFt (comme indiqué dans le tableau 3.1). La constante de vitesse de réaction normalisée la plus élevée ($12{,}9 \times 10^{-4}$ min^{-1} mg^{-1}) obtenue par $ZnIn_2S_4$-TiO_2 NFts est 1,3 fois plus élevée que celle ($9{,}8 \times 10^{-4}$ min^{-1} mg^{-1}) par $ZnIn_2S_4$.

Lorsque le système réactionnel est exposé à la lumière solaire, les NFts $ZnIn_2S_4$-TiO_2 présentent toujours une activité photocatalytique plus élevée que tous les autres photocatalyseurs (figure 0.9c, d). La constante de vitesse calculée à partir du modèle de réaction du premier ordre suit l'ordre : $ZnIn_2S_4$-TiO_2 NFts> $ZnIn_2S_4$ + P25> $ZnIn_2S_4$> $ZnIn_2S_4$ + TiO_2 NFts> $ZnIn_2S_4$-P25> P25> TiO_2 NFt (comme illustré dans le tableau 3.2). La constante de vitesse de réaction normalisée la plus élevée ($19{,}5 \times 10^{-3}$ min^{-1} mg^{-1}) obtenue par $ZnIn_2S_4$-TiO_2 NFts est 2,5 fois plus élevée que celle ($7{,}6 \times 10^{-3}$ min^{-1} mg^{-1})

par $ZnIn_2S_4$ et 2.7 fois plus élevée que cela (7,0 x 10^{-3} min^{-1} mg^{-1}) par $ZnIn_2S_4$ + TiO_2 NFts. La plus grande activité photocatalytique a été obtenue par les photocatalyseurs hybrides $ZnIn_2S_4$-TiO_2 NFt, indiquant que le $ZnIn_2S_4$ pourrait jouer un rôle important dans la formation de l'hétérojonction résultant en une photocatalyse améliorée bien supérieure au mélange de $ZnIn_2S_4$ et TiO_2 NFts.

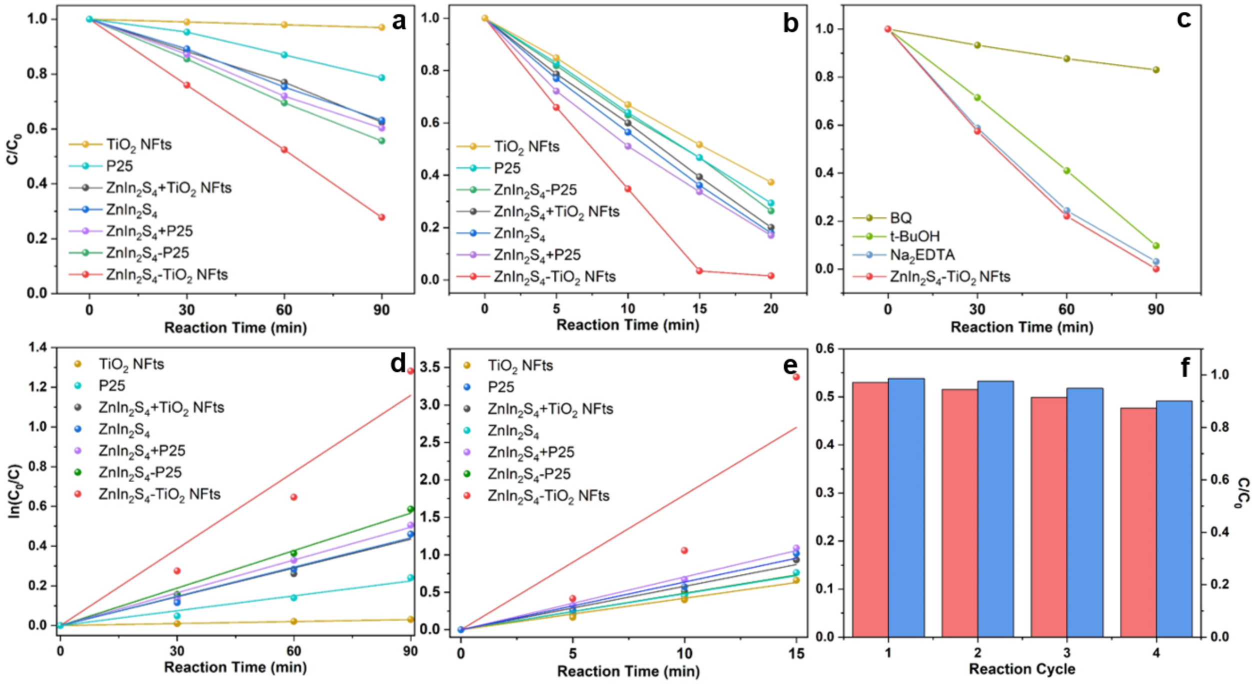

Figure 0.9 L'intrigue (a) et l'étude cinétique (d) de la MO dépendante du temps pour 10 mg de chaque photocatalyseur dans 25 ml de dégradation de la solution MO à 30 mg/L sous irradiation visible avec un filtre de 420 nm. L'intrigue (b) et l'étude cinétique (e) de la MO dépendante du temps pour 10 mg de chaque photocatalyseur dans 25 ml de dégradation de la solution MO à 30 mg/L sous spectre solaire. Le tracé (c) des expériences de piégeage et l'histogramme (f) de la mesure de la durabilité pour 10 mg de photocatalyseurs ZnIn2S4-TiO2 NFts dans 25 ml de solution de dégradation de 30 mg/L MO sous irradiation visible avec un filtre de 420 nm pendant 60 min à chaque fois et sous irradiation solaire pendant 15 min à chaque fois.

Après avoir effectué quatre passages successifs sous lumière visible et éclairage solaire simulé, presque aucun changement d'activité n'est trouvé pour le photocatalyseur $ZnIn_2S_4$-TiO_2 NFt, et la performance de dégradation de MO reste toujours supérieure à 85% (Figure 0.9f). Les performances élevées et la stabilité élevée des photocatalyseurs tels que synthétisés sous lumière visible et lumière solaire sont bénéfiques pour l'application à grande échelle de la photocatalyse dans la dépollution de l'environnement en utilisant une énergie solaire abondante.

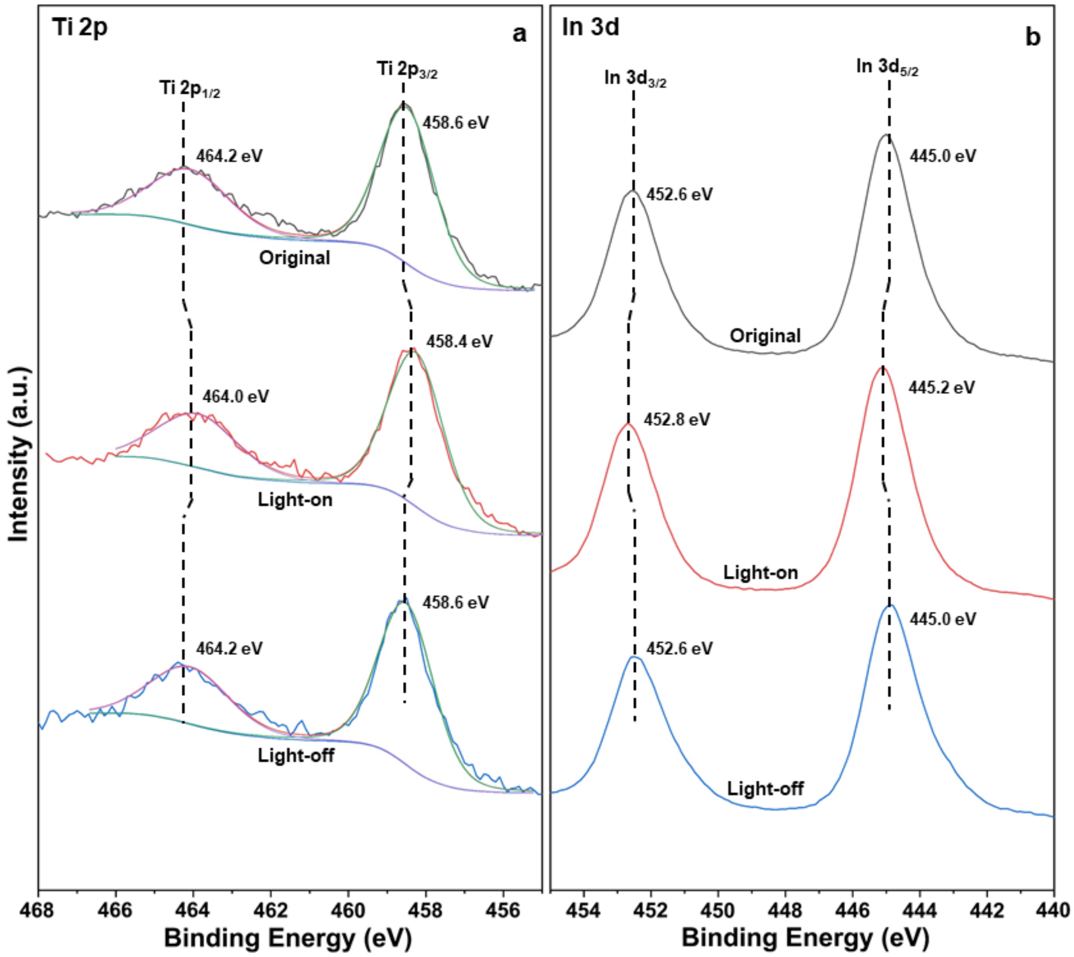

Figure 0.10 Spectres XPS Ti 2p (a) et In 3d (b) haute résolution des $ZnIn_2S_4$-TiO_2 NFts.

Pour élucider si le transfert de charge interfaciale entre TiO_2 et $ZnIn_2S_4$ est conforme à la voie d'hétérojonction de type II, une caractérisation ISI-XPS a été réalisée (Figure 0.10) [99]. Sans irradiation lumineuse, le $ZnIn_2S_4$-TiO_2 NFts présentait deux pics à 458,6 (Ti $2p_{3/2}$) et 464,2 eV (Ti $2p_{1/2}$) attribués au TiO_2. Lors d'une irradiation lumineuse, il y avait un léger décalage négatif (de -0,2 eV) dans l'énergie de liaison Ti 2p, suggérant une diminution de sa densité électronique sous irradiation lumineuse. Pendant ce temps, deux pics caractéristiques attribués au $ZnIn_2S_4$ à 445,0 (In $3d_{5/2}$) et 452,6 eV (In $3d_{3/2}$) ont été observés sans lumière, qui ont subi un décalage positif (de 0,2 eV) sous irradiation lumineuse, suggérant une augmentation de l'électron densité sur le TiO_2. Ces déplacements d'énergie de liaison fournissent une preuve directe de la voie de migration des porteurs de charge à travers l'interface $ZnIn_2S_4$-TiO_2 NFts dans les mêmes conditions d'irradiation lumineuse que la réaction photocatalytique. Dans le détail, les électrons photogénérés migrent de $ZnIn_2S_4$ vers TiO_2, ce qui est en bon accord avec le mécanisme de type II (Figure 0.11).

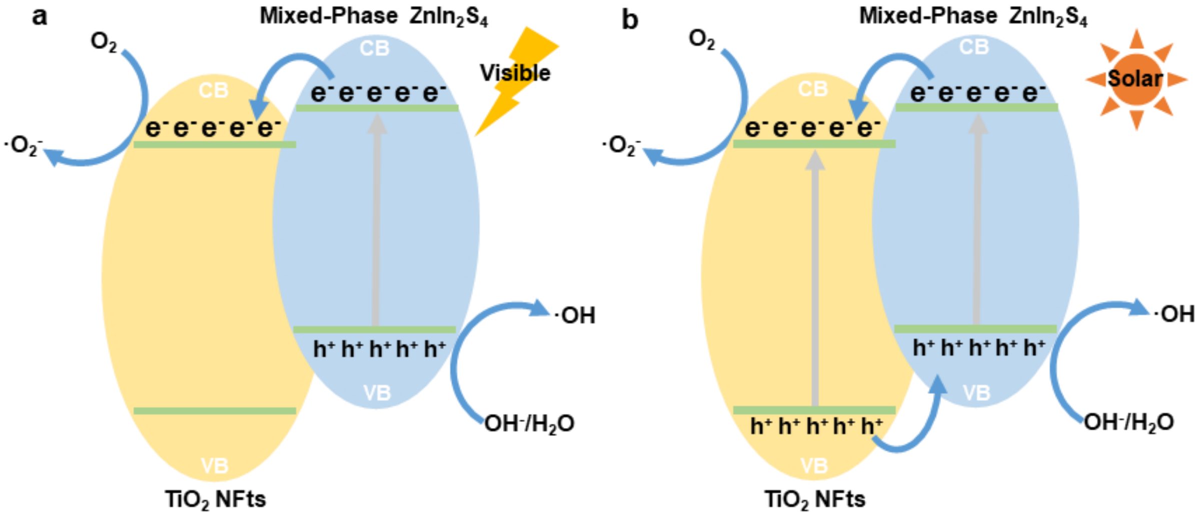

Figure 0.11 Mécanisme photocatalytique proposé des photocatalyseurs $ZnIn_2S_4$-TiO_2 NFt sous (a) lumière visible ($\lambda > 420$ nm) et (b) irradiation solaire, respectivement.

En résumé, des preuves solides basées sur la caractérisation ISI-XPS et l'expérience de piégeage confirment la formation de l'hétérojonction de type II entre TiO_2 et $ZnIn_2S_4$. La formation d'hétérojonction de type II peut grandement améliorer l'utilisation des électrons et des trous photogénérés avec des capacités de réduction et d'oxydation élevées, respectivement. En conséquence, les performances de dégradation photocatalytique des MO du composite $ZnIn_2S_4$-TiO_2 NFts étaient significativement supérieures à celles du $ZnIn_2S_4$, des TiO_2 NFts, du TiO_2 commercial (P25) et d'autres échantillons comparatifs pour la photodégradation. Ce travail confirme de manière exhaustive la présence des excellents NFt $ZnIn_2S_4$-TiO_2 à travers des analyses expérimentales et théoriques, fournissant une inspiration importante pour le développement futur de composites semi-conducteurs dans une utilisation efficace de l'énergie solaire, répondant largement aux exigences de l'application environnementale.

0.5 CONCLUSION

En utilisant l'effet positif des nanoforêts tridimensionnelles de TiO_2 hiérarchiquement structurées sur le transfert de porteurs pour surmonter la recombinaison ultrarapide des porteurs de $ZnIn_2S_4$, une plage de réponse lumineuse considérablement élargie et une activité photocatalytique améliorée sont obtenues. Pendant ce temps, la combinaison des phases hexagonales et cubiques de $ZnIn_2S_4$ améliore encore l'absorption lumineuse du photocatalyseur. Dans ce travail, les $ZnIn_2S_4$-TiO_2 NFts ont été produits par une méthode hydrothermale simple. Le photocatalyseur synthétisé a montré une excellente activité dans la dégradation photocatalytique de MO. Selon les propriétés optiques et les expériences de photodégradation sous différentes irradiations lumineuses, la dynamique a été étudiée. On constate que la constante de vitesse du photocatalyseur obtenu est supérieure à d'autres photocatalyseurs comparatifs dans la région de la lumière visible, tandis que sa constante de vitesse est augmentée à trois fois celle de $ZnIn_2S_4$ sous le spectre solaire, ce qui indique que le photocatalyseur développé, $ZnIn_2S_4$-TiO_2, répond largement aux exigences de l'application environnementale.

CONTENTS

LISTE DES TABLEAUX

LISTE DES FIGURE

1 INTRODUCTION

1.1 General context

Nowadays, with the rapid development of social industrialization and population growth in modern society, a large number of harmful and toxic pollutants are released into the ecological environment around us [1-3]. Therefore, serious environmental pollution and increasing energy demand have become two major global problems in the current era. Fortunately,more and more attention is focused on exploring green and environmentally friendly technologies to ensure the sustainable and healthy development of all mankind. Among current technologies, semiconductor-based photocatalysis is considered to be one of the most promising clean technologies for dealing with global environmental pollution [4,5]. Semiconductor photocatalysis technology can repair the environment by photocatalytic degradation of various harmful and toxic pollutants [6-10].

Over the past two decades, there have been huge efforts on the smart design of nanostructured materials for photocatalysis [11-23]. Among various promising photocatalysts, titanium dioxide (TiO_2) is a preferred one and has been more widely developed than all other reported materials on account of its unique and diverse favorable properties including (i) allowing manipulation of its morphology, (ii) strong Ti-O chemical bonds for excellent long-term stability and photo-corrosion resistibility, (iii) low toxicity and environmentally friendly nature, (iv) facile availability due to abundant precursors, (v) bandgap with 3.0-3.2 eV and high oxidization.

However, the wide band gap (3.2 eV) prevents TiO_2 from meeting the requirements of practical applications because it can only respond to ultraviolet or near-ultraviolet light, resulting in low solar energy utilization efficiency [25]. Therefore, in order to make better use of solar energy, the development of visible light irradiation photocatalysts has attracted widespread attention. So far, researchers have developed or invented various photocatalysts irradiated by visible light, such as TiO_2, simple oxide Fe_2O_3 [26], composite oxide Ag_3PO_4 [27] , Bi_2MoO_6 [28] and Bi_2WO_6 [29], metal chalcogenide CdS [30] and so on. Among these visible light-responsive catalysts, metal sulfur compounds have been extensively studied due to their unique photoelectrocatalytic properties and relative chemical stability. In addition, new ternary metal chalcogenides have attracted widespread attention in recent years [31].

Zinc indium sulfide ($ZnIn_2S_4$) is a typical ternary metal sulfide with excellent photocatalytic performance. It has a layered structure and can present three different crystal forms, including cubic phase, hexagonal phase and rhombohedral phase. Each crystal form of $ZnIn_2S_4$ exhibits photocatalytic performance under visible light irradiation. Based on the layered structure, researchers have successfully synthesized $ZnIn_2S_4$ micro/nano structures with different morphological characteristics. $ZnIn_2S_4$ has a suitable forbidden band width. There is a positive response in the visible light region [32-35]. At the same time, compared with traditional metal sulfides such as CdS [30] and Sb_2S_3 [36], $ZnIn_2S_4$ is less toxic and shows similar optical properties, which shows that it has a wide range of applications in environmental protection and other ternary metal chalcogenides such as $CuGaS_2$ [37] and compared with $ZnIn_2S_4$ [38], $ZnIn_2S_4$ has a wide range of sources, simple chemical composition, relatively easy preparation, and shows considerable chemical stability in the photocatalytic process [39]. Therefore, $ZnIn_2S_4$ has attracted widespread attention due to its attractive physical and chemical properties, as well as low cost, low toxicity and easy preparation. Based on the above advantages, $ZnIn_2S_4$ has broad application prospects in the fields of hydrogen evolution, CO_2 reduction, selective organic synthesis and environmental protection under visible light.

This thesis focus on suppressed recombination of photogenerated electrons and holes, for $ZnIn_2S_4$ in hexagonal families, utilizing the positive effect of hierarchical TiO_2 including rapid electron transfer, long electron lifetime, and diffusion length of charge carriers, to develop a broadband photocatalyst for environmental remediation.

This manuscript is divided into 3 distinct chapters:

- The first chapter will detail the structure, properties, and modification of TiO_2 and $ZnIn_2S_4$

- The second chapter is devoted to all the tools for preparing and characterizing TiO_2.

- The third chapter will present the experimental results obtained and analyze its structural features, optical properties, and photocatalytic performance.

1.2 Structure, properties and modification of titanium dioxide

1.2.1 Crystal structure of TiO_2

TiO_2 exists 3 phases in nature: rutile (tetragonal), anatase (tetragonal), and brookite (orthorhombic), where there are 2 most common phases of anatase and rutile because of brookite possessing poor crystallographic symmetry and weak thermal stability. All of these phases can be described as an arrangement of slightly distorted TiO_6 octahedra, connected by vertices or ridges, while oxygen shows triple coordination [11]. These 3 crystal structures are shown in Figure 1.1.

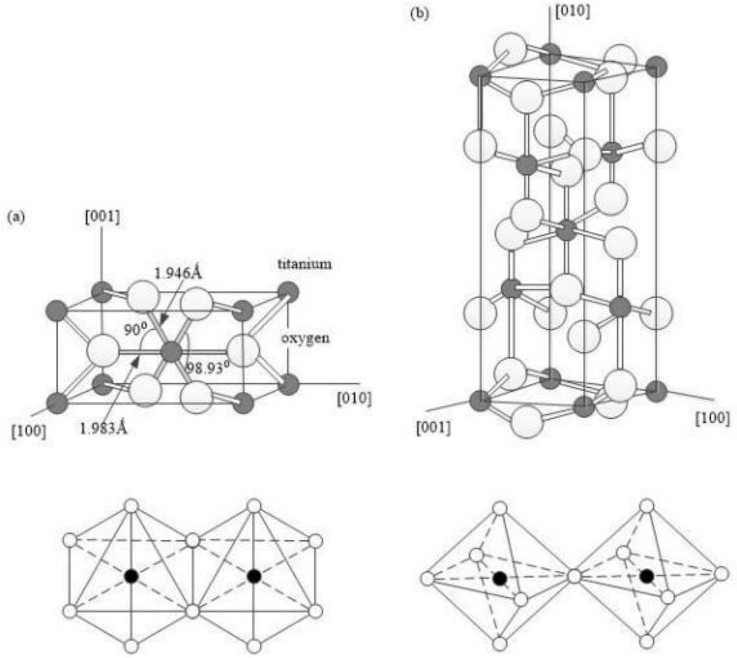

Figure 1.1 Crystal structure of (a) rutile and (b) anatase.

Rutile is denser (4.250 g/cm^3) than anatase (3.894 g/cm^3). Although the rutile phase is the most stable of all (at pressures below 60 kPa), the difference in internal energy with the anatase phase is small, indicating that the anatase phase is a metastable phase. Therefore, TiO_2 anatase can be easily obtained by synthesis at low temperature (below 400 °C), while the rutile phase, depending on the pressure conditions, begins to appear between 400 and 600 °C, and becomes the dominant phase at temperatures above 600 °C.

Although the bandgap of the rutile phase is smaller than that of the anatase phase (as shown in Table 1.1), the photoelectrolytic efficiency is greater for the anatase phase. Several explanations exist for this counter-intuitive fact: difference in Fermi levels, mobility of charge carriers, or an increased concentration of hydroxyl radical for the anatase phase. Luttrell et al. suggest that the difference is mainly due to the mobility of the charge carriers. Meanwhile, the larger bandgap of the anatase with 3.2 eV provides a stronger oxidizing ability resulting in benefited to obtain a more thorough degradation of organic pollutants.

Table 1.1 Crystal structure data for TiO_2.

Phase	Rutile	Anatase	Brookite
Lattice system	Tetragonal	Ttetragonal	Orthorhombic
Lattice parameter	a=4.5936 Å c=2.9587 Å	a=3.784 Å c=9.515 Å	a=9.184 Å b=5.447 Å c=5.154 Å
Space group	P42/mnm	I41/amd	Pbca
Ti-O bond length	1.949(4) Å 1.908(2) Å	1.937(4) Å 1.965(2) Å	1.87-2.04 Å
O-Ti-O bond angle	81.2° 90.0°	77.7° 92.6°	77.0°-105°
Bandgap	3.02 eV	3.20 eV	2.96 eV

1.2.2 Electronic band structure of TiO_2

The electronic band structure of semiconductor materials generally consists of a low-energy valence band (VB) filled with electrons and an empty high-energy conduction band (CB). The part from the bottom of the conduction band to the top of the valence band is called the bandgap (Eg), which is numerically equal to the energy level difference between the conduction band and the valence band.

TiO_2 is a semiconductor material with a broad bandgap. The bandgaps of anatase, brookite, and rutile are 3.20 eV, 2.96 eV, and 3.02 eV, respectively.

When the photon energy of the TiO_2 semiconductor photocatalytic material is greater than the bandgap, the electrons in the valence band will jump to the conduction band when excited, making the O^{2-} in the valence band O^- and leaving the corresponding holes, Ti^{4+} in the conduction band becomes Ti^{3+} photogenerated electrons, thus forming electron-hole pairs. Photo-generated holes have strong oxidizing capability, which can absorb and capture electrons on the surface of semiconductors or in solvents, causing them to be oxidized; photo-generated electrons have strong reducing capability, which can make the electron acceptor on the semiconductor surface accept electrons and be reduction. The photo-generated electrons and holes form a redox system.

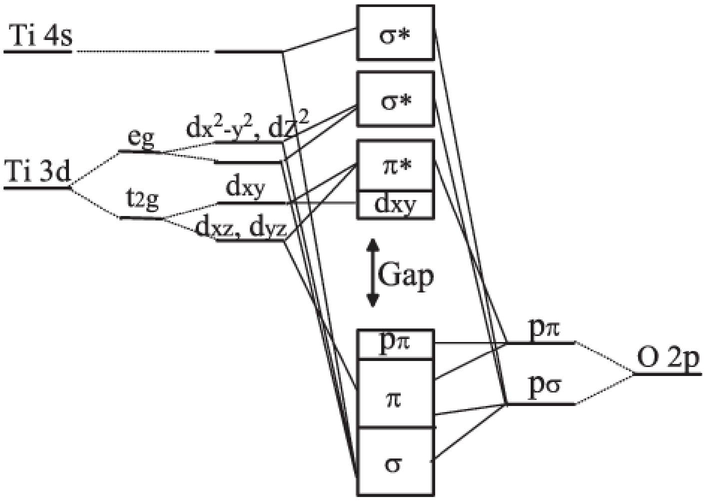

Figure 1.2 Electronic band structure of anatase.

TiO_2 is an N-type semiconductor. Figure 1.2 shows that the BV (valence band) is predominantly dominated by the 2p orbital of the O atom. The 3d orbital of the Titanium atom is at bottom of the BC (conduction band). This presence of oxygen in BV justifies the fact that TiO_2 is an N-type semiconductor because for each oxygen missing in the structure, there are 2 free electrons compensated by the Ti^{3+} centers.

For the anatase phase, the bandgap is 3.2 eV, which means that TiO_2 anatase absorbs photons with a wavelength less than or equal to 380 nm. TiO_2 anatase, therefore, absorbs in the UV region of the solar spectrum, which corresponds to less than 5% of solar energy.

1.2.3 The photocatalytic mechanism of TiO_2

As shown in Figure 1.3 [12-14], light with energy greater than the forbidden band width of TiO_2 will excite electrons (e^-), and the photogenerated electrons will transition from the valence band to the conduction band, leaving a void in the valence band. Hole (h^+), forming a photo-generated electron-hole pair. Due to the discontinuity of the forbidden band of TiO_2, it can prevent the recombination of photo-generated electrons and holes, and cause the electrons and holes to undergo oxidation-reduction reactions with the substances adsorbed on the surface. The total reaction process is shown in the table below.

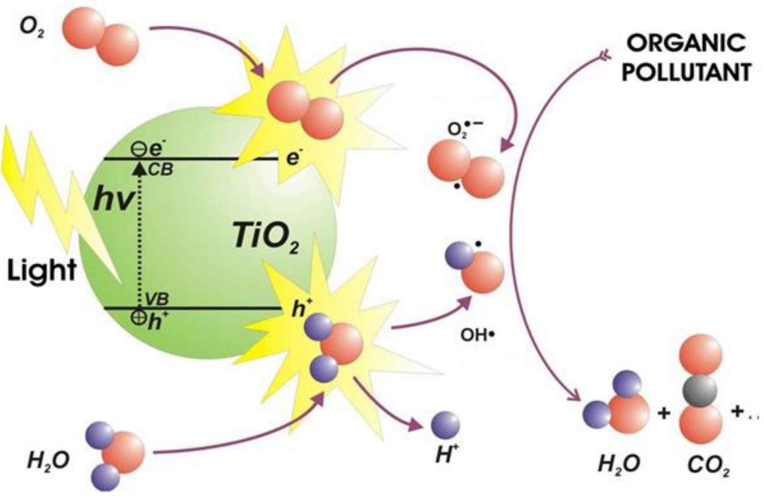

Figure 1.3 Photocatalytic mechanism of TiO_2.

1.2.4 The effect of grain size for photocatalysis

The grain size is an important indicator to measure the photocatalytic performance of nano-scale photocatalytic materials [15,16]. It is shown that nano-sized TiO_2 has enchaned photocatalytic performance. Because of its tiny size, photo-generated electrons and holes are easily separated, thereby reducing the recombination rate, resulting in the higher photocatalytic activity. When the radius of the nano-TiO_2 particles is close to 10 nm, the quantum size effect will occur, shortening the migration time of photo-generated electron-hole pairs on the catalyst surface to 10^{-11}s. The generation of quantum size effect will make the conduction band and valence band of TiO_2 become separate energy levels, the forbidden band width becomes wider, the conduction band potential is more negative, the valence band potential is more positive, and its spectral absorption band is red-shifted, making it more Strong redox ability. In addition, the smaller the size of the TiO_2 semiconductor, the higher the charge transfer rate. When the particle radius of the semiconductor is smaller than the thickness of its space charge layer, photo-generated carriers can migrate from the interior of the ion to the surface for direct diffusion, thereby increasing the diffusion rate of electrons and holes, effectively reducing their recombination rate, and improving the photoelectric conversion efficiency.

1.2.5 The influence of specific surface area for photocatalysis

The specific surface area is also an important criterion to measure the photocatalytic performance of semiconductor materials, and it determines the capabblity of pollutants adsorbed by the photocatalytic material. The increase in specific surface area can provide continuous photocatalytic reaction sites and sufficient surface-active sites for the degraded substances. The hierarchically structured TiO_2 photocatalyst can adsorb more organic pollutants due to its larger specific surface area, so that the pollutant molecules can fully contact the catalytic material, increase the adsorption capacity and accelerate the interface reaction speed, and finally improve the photocatalytic performance.

1.2.6 Separation of photogenerated electron-hole pairs

As mentioned in chapter 1.2.2, TiO_2 is an N-type semiconductor. When it is irradiated by light with energy equal to or greater than the band gap energy, the electrons in the valence band gain energy and jump to a higher energy level. The electrons after the transition are not stable and will quickly release the acquired energy back to the original Energy level. Only when the energy gained by the electrons is high enough can they get rid of the bondage of the nucleus and become free electrons, so that the electrons in the valence band will be vacated to form holes. The greater the number of electron-hole pairs formed, the better the photocatalytic performance. Therefore, one of the ways to improve photocatalytic performance is to prevent the recombination of photogenerated electron-hole pairs.

1.2.7 Heterojunction construction of TiO_2

Heterojunction construction refers to the combination of semiconductors with different bandgaps. The difference in energy levels can promote the separation of photogenerated electron-hole pairs, broaden the light response range, and effectively utilize solar energy. Because of its wide light response range, the narrow band gap semiconductor is first excited to generate electrons, which migrate to the conduction band of TiO_2 due to its low conduction band potential, thus realizing the separation of photogenerated electron-hole pairs.

There are many semiconductors compounded with TiO_2, such as Cds [22], ZnO [23,24], SnO_2 [25,26], SiO_2 [27,28], WO_3 [29], V_2O_5 [30], La_2O_3 [31] and C_3N_4 etc. Among them, the CdS-TiO_2 [32.33] system has been studied in depth as a typical compound semiconductor. As a representative of a novel non-metallic nitride, C_3N_4 is a semiconductor material with a graphene-like framework. Li et al. [34] prepared a series of CdTe-composited TiO_2 nanocatalysts of different sizes by sol-gel method, and the results showed that the visible light response range of the composite catalyst was broadened, and the dye was completely degraded after 4 hours of illumination. Liang Wenzhen et al. [35] prepared TiO_2/SiO_2 aerogel composite photocatalyst by doping silica aerogel into TiO_2 sol by sol-gel method and atmospheric drying method. The results show that the adsorption rate and photodegradation rate of the doped photocatalyst to the 2,4-dinitrophenol solution are significantly better than that of the pure TiO_2 sample, and the catalytic activity after the composite is greatly improved. Sun et al. [36] produced CdS/TiO_2 electrodes and applied them to solar cells. Compared with the uncomposited TiO_2 nanotube electrode, the photocurrent of the CdS/TiO_2 electrode is increased by 35 times. $ZnIn_2S_4$ is a kind of light-conducting material with high application prospects, which has attracted widespread attention in the application of photocatalytic hydrogen production and photocatalytic degradation of organic pollutants. Its band gap is in the range of 2.1~2.8 eV, with strong light absorption performance and excellent photocatalytic stability. Studies have shown that by combining wide band gap TiO_2 and narrow band gap $ZnIn_2S_4$ semiconductors, a new type of composite semiconductor material that responds to both ultraviolet and visible can be obtained, and has good photocatalytic activity.

1.2.8 Element doping for TiO_2

The doped non-metallic elements (such as C, N, S, F, etc.) will replace O^{2-}, Ti^{4+} in TiO_2 to form a doped energy level close to the valence band, thereby reducing the band gap of TiO_2. The light response range extends from the ultraviolet light region to the visible light region. Doping of non-metallic elements is one of the effective ways to improve the visible light response of TiO_2. In 2001, Asahi et al. [37] prepared a N-doped TiO_2 composite film, and their study showed that the photocatalytic activity of the N-doped composite film was significantly improved. The principle is that doped N replaces the lattice oxygen of TiO_2, narrowing the forbidden band width of TiO_2, and making it visible light active. He believes that the following requirements must be met to have visible light activity: the impurity level that can absorb visible light is introduced and formed after doping; the minimum energy level of the conduction band including the secondary impurity level should be maintained at the same energy level as TiO_2 or The energy level is higher than that of water to maintain the photocatalytic reduction ability of the catalyst; the impurity energy level and the TiO_2 energy level should overlap to ensure that the photogenerated carriers move quickly and reach the catalyst surface in a short time.

Umebayashi et al. produced S-doped TiO_2 by calcination, which still responded at wavelengths greater than 420 nm, and used XRD and XPS characterization methods to prove that the valence state of S in the composite material was -2, which replaced the oxygen lattice in TiO_2. Zhang et al. [38] used a one-step hydrothermal method to successfully prepare a P25/graphene composite catalyst using P25 and graphene oxide as raw materials. The photocatalytic effect is improved. Zaleska et al. used mechanical grinding and sol-gel methods to prepare boron-doped titanium dioxide catalysts using boric acid and ethyl borate as boron sources. Studies have pointed out that an appropriate amount of boron will expand the light response range of TiO_2 and increase the photocatalytic activity.

Doping metal cations in TiO_2 semiconductors can control the electronic structure of TiO_2. On the one hand, introducing lattice defects or changing the crystallinity, providing more oxygen vacancies in order to effectively capture electrons or holes to increase the migration rate of surface charges, thereby extending the life of electron-hole pairs, and achieving the purpose of improving photocatalytic performance On the other hand, when the doped metal ions exceed a certain amount, it can not only inhibit the phase transition of TiO_2, but also may become the electron-hole recombination center. Therefore, the doping of an appropriate amount of metal ions can not only promote the separation of photo-generated carriers, but also broaden the light response range, and use more visible light to achieve a better photocatalytic effect.

As early as 1990, Verwey et al. incorporated metal ions of different valence states into semiconductors and found that the photocatalytic properties of the semiconductors were improved after doping. Choi W et al. [39] used the sol-gel method to dope TiO_2 with different metal ions. After studying the photocatalytic effect of doping with different metal ions, it is found that various factors such as ion species, doping amount, ion distribution, etc. will affect the photocatalytic activity of TiO_2. The results show that Fe^{3+}, V^{4+}, Re^{5+}, Mo^{5+}, Ru^{2+}, Os^{2+} and Rh^{2+} plasma can improve the photocatalytic performance of titanium dioxide. Lu Weiqi et al. [40] used the degradation of rhodamine B as a performance test method to study the synthesized Gd^{3+} and La^{3+} co-doped nano-TiO_2. The result is that the degradation effect is the best when the doping amount is 0.5%.

1.3 Structure, properties and modification of zinc indium sulfide

1.3.1 Structural properties of $ZnIn_2S_4$

$ZnIn_2S_4$ has a layered structure, which can form two types of crystal families and three different lattice systems (Table 1.2), including cubic lattice, hexagonal lattice and rhombohedral lattice [40]. As shown in Figure 1.4, the atoms are arranged in S-In-S-In-S-Zn-S layer. Regarding the cubic crystal form of $ZnIn_2S_4$, it is a direct cubic spinel phase with ABC packing of S atoms. The Zn atom is tetrahedral coordinated with the S atom, and octahedral coordinated with the In atom. The hexagonal crystal type of $ZnIn_2S_4$, a layer with strong In-S bonds and Zn-S bonds in the layered compound layer, and weak S-S bonds between S atoms belonging to different layers. In the hexagonal crystal system, S atoms are tetrahedral coordinated around zinc atoms, and tetrahedral or octahedral coordinated around In atoms. After research, hexagonal $ZnIn_2S_4$ and cubic $ZnIn_2S_4$ are more commonly discussed than diamond $ZnIn_2S_4$. Different crystal types of $ZnIn_2S_4$ have different characteristics. According to reports, the hexagonal $ZnIn_2S_4$ has photoluminescence [41] and photoconductivity [42]. In addition, both the hexagonal and cubic $ZnIn_2S_4$ have photocatalytic hydrogen evolution and pollutant removal activities, while the hexagonal $ZnIn_2S_4$ has better performance [34, 43].

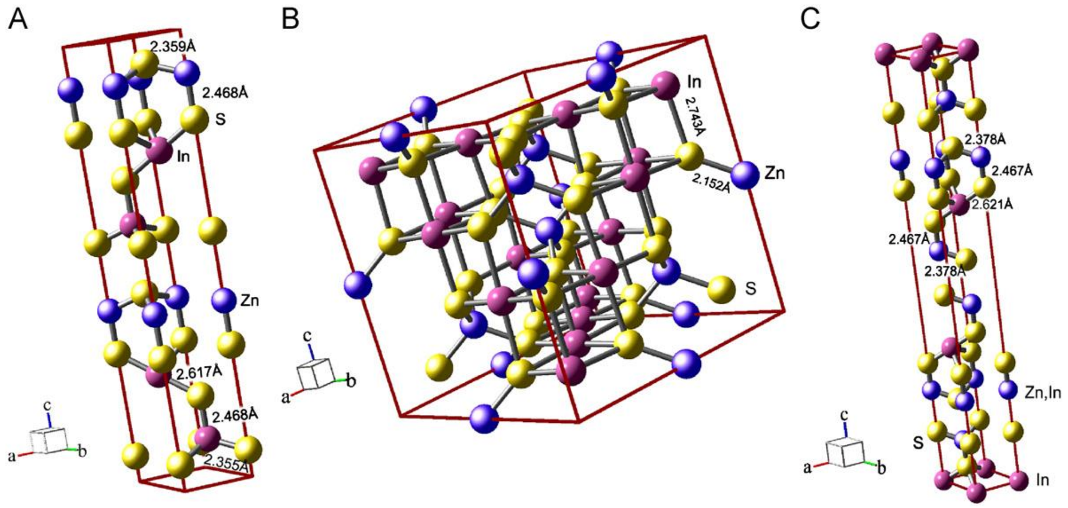

Figure 1.4 Crystal structures of (A) hexagonal, (B) cubic and (C) rhombohedral $ZnIn_2S_4$ [40].

Table 1.2 Crystal structure data for $ZnIn_2S_4$.

Crystal family	Hexagonal		Cubic
Lattice system	Rhombohedral	Hexagonal	Cubic
Lattice parameter	a=3.8656 Å c=37.0063 Å	a=3.85 Å c=24.68 Å	a=10.6211 Å
Space group	R-3m	P63mc	Fd-3m
Bandgap	2.5 eV	2.32 eV	2.25 eV

Based on the layered crystal structure, different sizes and shapes of $ZnIn_2S_4$ were synthesized, as shown in Figure 1.5, including zero-dimensional (such as nanoparticles and quantum dots), one-dimensional (such as nanotubes, nanoribbons, and nanowires [39]), and two-dimensional (Such as nanosheets [44], microspheres composed of flakes and films [45]) and three-dimensional (such as flower-like/porous/hollow microspheres and flower balls [46]). In general, the shape and size of a semiconductor will have an important impact on its performance. $ZnIn_2S_4$ has surface defects, while the zero-dimensional $ZnIn_2S_4$ with small quantum size (nanoparticles and quantum dots) can inhibit the recombination of electron-hole pairs in surface defects due to uniform distribution and sufficient shrinkage. In addition, the morphology of one-dimensional $ZnIn_2S_4$ is conducive to the separation of photogenerated electron-hole pairs. For the two-dimensional $ZnIn_2S_4$ nanostructure, compared with the bulk $ZnIn_2S_4$, the flaky $ZnIn_2S_4$ has a higher specific surface area, more surface atoms, and therefore more active centers. The three-dimensional $ZnIn_2S_4$ usually has a spherical or flower-like structure, which can provide more active sites, which has advantages in functional applications.

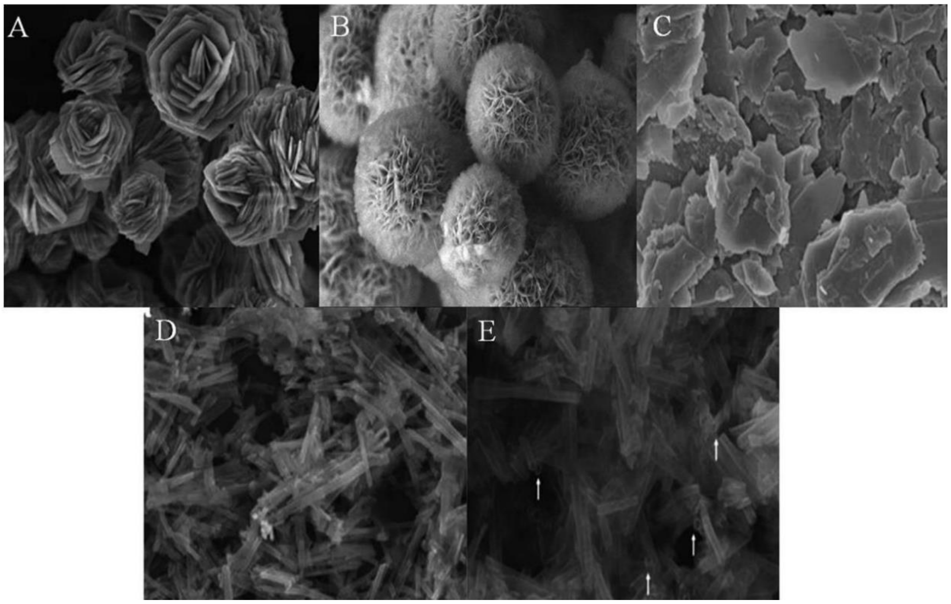

Figure 1.5 (A)Rose flower-like structures. (B) Marigold like microspheres (C) Nanosheets. (D) Nanowires. (E) Nanotubes [39-64].

1.3.2 Electronic and optical properties of $ZnIn_2S_4$

$ZnIn_2S_4$ has excellent electronic and optical properties, and has an adjustable band gap (2.06-2.85 eV) [35,39]. $ZnIn_2S_4$ crystal is a direct band gap semiconductor, and its band structure can be calculated by density functional theory (DFT) [47]. Generally, when conducting a semiconductor band gap simulation, the limitation of the approximation function will make the estimated value low. Therefore, the calculated band gaps of the hexagonal and cubic $ZnIn_2S_4$ are 0.28 and 1.36 eV, respectively, which are lower than the experimental values [44]. The light absorption edge of $ZnIn_2S_4$ is in the visible light region (about 570 nm). Under visible light, $ZnIn_2S_4$ has broad application prospects in energy conversion and pollutant removal.

Generally, the optical response of a semiconductor depends to a large extent on its basic electronic properties, which are closely related to the chemical or ionic, atomic arrangement and physical size of nanomaterials. For example, Chen et al. compared the optical properties of cubic and hexagonal $ZnIn_2S_4$ prepared by hydrothermal methods [48]. The results show that the light absorption edges of hexagonal and cubic $ZnIn_2S_4$ are 490 nm and 538 nm, respectively. The results show that when the crystallinity of $ZnIn_2S_4$ changes from hexagonal to cubic, the absorption edge will have a red shift, indicating that cubic $ZnIn_2S_4$ has better light absorption ability, confirming the influence of crystallinity.

1.3.3 Structure and morphology control of $ZnIn_2S_4$

Although the band gap of $ZnIn_2S_4$ is suitable for hydrogen evolution from water, $ZnIn_2S_4$ still has problems such as structural defects, unsatisfactory separation efficiency and poor photo-generated carrier mobility. Therefore, many strategies have been proposed to improve the photocatalytic performance of $ZnIn_2S_4$, including structure and morphology control and surface modification. These strategies can change the surface and optical properties of semiconductors, accelerate charge transfer, reduce charge recombination rate, and improve photocatalytic performance.

The structure and morphology of the semiconductor have an important influence on its photocatalytic performance. Controlling the structure and morphology of the catalyst is an effective way to improve the photocatalytic hydrogen production of $ZnIn_2S_4$. For example, Shen et al. studied the effect of crystallinity [49]. The flowering cherry-like microspheres $ZnIn_2S_4$ were synthesized under the reaction conditions of water as solvent, and microclusters $ZnIn_2S_4$ were synthesized in organic solvent. Flowering cherry-like microspheres $ZnIn_2S_4$ have a compact structure and good crystallinity. The results show that the better the crystallinity, the better the hydrogen evolution performance. In addition to the crystal structure, the morphology also has an effect on the photocatalytic activity. For example, Bai et al. reported that porous $ZnIn_2S_4$ microspheres exhibited better photocatalytic performance than bulk $ZnIn_2S_4$ in terms of hydrogen evolution [50]. The pore structure, large specific surface area, and high volume ratio can effectively inhibit electron-hole recombination and promote charge transfer, which is beneficial to photocatalytic activity. In addition, specific surface area and porosity are non-negligible factors that affect photocatalytic performance. In order to obtain $ZnIn_2S_4$ micro/nano structures with different morphological characteristics under mild conditions, different synthesis methods have been developed, including hydrothermal [51-53], solvothermal [32,49,45], and microwave-assisted methods [33].

1.3.4 Element doping of $ZnIn_2S_4$

On the one hand, element doping can narrow the band gap and improve light absorption. On the other hand, doping can also accelerate the interface charge transfer, inhibit the recombination of photogenerated electron-hole pairs, and provide more defects. In addition, the structure and shape of semiconductors can be adjusted by introducing elements. Therefore, the doping of elements in the micro-nano structure $ZnIn_2S_4$ to improve the performance of photocatalytic water hydrogen evolution has been extensively studied.

In order to improve the optical and electronic properties of $ZnIn_2S_4$, researchers doped transition metal ions. For example, Shen et al. synthesized a copper-doped $ZnIn_2S_4$ sample by a simple hydrothermal method, and photodeposited Pt (1wt%) on the photocatalyst as a cocatalyst [47]. According to the XRD characterization given in Figure 1.7 (A-B), it was confirmed that copper ions were introduced into the $ZnIn_2S_4$ lattice. In addition, as the Cu content changes in the range of 0-2.0wt%, the diffraction peak intensity changes. As shown in Figure 1.7A, $ZnIn_2S_4$ doped with 0.5wt% copper has the highest photocatalytic activity, and the hydrogen evolution rate is 757.5umol/g·h, which is 5.85 times that of undoped $ZnIn_2S_4$. The quantum yield increased from 9.6% to 14.2%. The band gap narrowed from 2.51 eV to 1.91 eV, indicating a wider light absorption. As shown in Figure 1.7B, with the increase of Cu ions, the absorption edge of Cu-$ZnIn_2S_4$ shifts from 495nm to 650nm. Due to the introduction of copper ions, the forbidden band width becomes narrower, light absorption becomes wider, vacancies increase, and photocatalytic activity is enhanced. In addition to transition metal ion doping, Tian et al. studied the photocatalytic activity of rare earth ions La^{3+}, Ce^{3+}, Gd^{+}, Er^{3+} and Y^{+} doped with $ZnIn_2S_4$ [54]. Shen et al. used a microwave-assisted hydrothermal method to prepare a series of alkaline earth metal (Ca, Sr and Ba) doped $ZnIn_2S_4$ photocatalysts [55]. The results show that compared with unmodified $ZnIn_2S_4$, the doping of metal ions improves the photocatalytic performance of $ZnIn_2S_4$ to a certain extent.

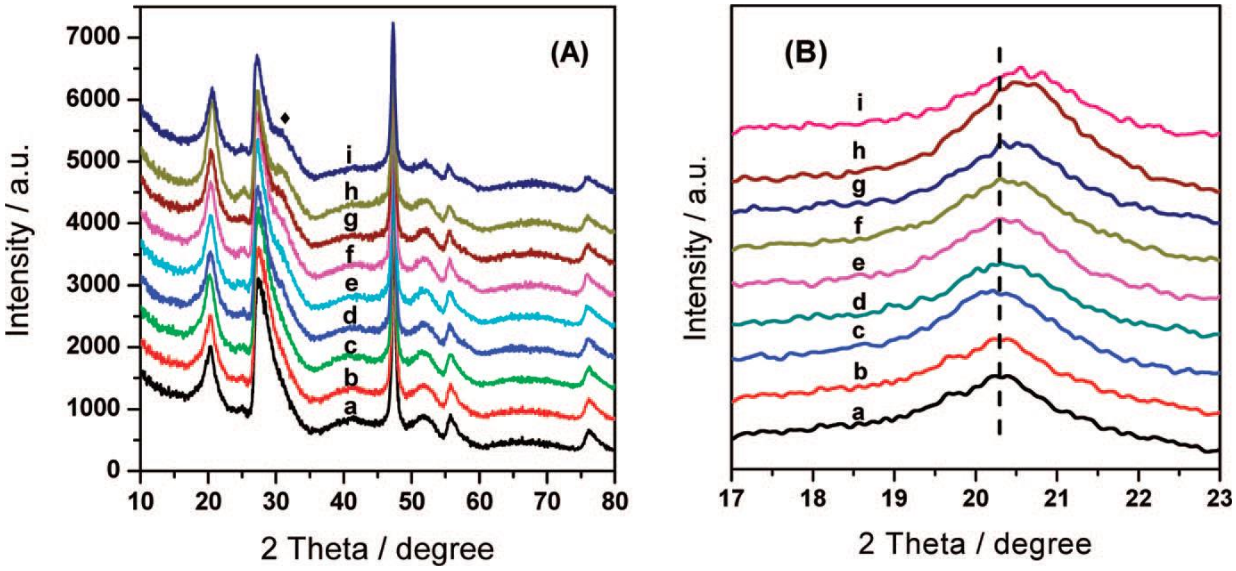

Figure 1.6 X-ray diffraction patterns of Cu(X)-$ZnIn_2S_4$; the values of X were (a) 0.0 wt%, (b) 0.1 wt%, (c) 0.3 wt%, (d) 0.5 wt%, (e) 0.7 wt%; (f) 0.9 wt%, (g) 1.2 wt%, (h) 1.6 wt%, (i) 2.0 wt% [47].

In addition to the doping of metal ions, Yang et al. also reported O-doped $ZnIn_2S_4$ and its excellent photocatalytic hydrogen evolution performance [56]. The results show that the hydrogen production rate of O-doped $ZnIn_2S_4$ can reach 2120umol/g·h. In addition to the doping of metal ions, Yang et al. also reported O-doped $ZnIn_2S_4$ and its excellent photocatalytic hydrogen evolution performance. The results show that the hydrogen production rate of O-doped $ZnIn_2S_4$ can reach 2120 μmol/g·h, which is a pure phase of $ZnIn_2S_4$ O-doped $ZnIn_2S_4$ CB, which is about 0.86 eV higher than the original $ZnIn_2S_4$. For O-doped $ZnIn_2S_4$, compared with the original $ZnIn_2S_4$, the increase of VB and the increase of CB minimum means higher mobility and better consumption of photo-generated holes. In addition, the CB edge potential of O-doped $ZnIn_2S_4$ increased, indicating that it has a strong reducing ability. Therefore, O doping optimizes the band structure of $ZnIn_2S_4$ and improves the photocatalytic performance.

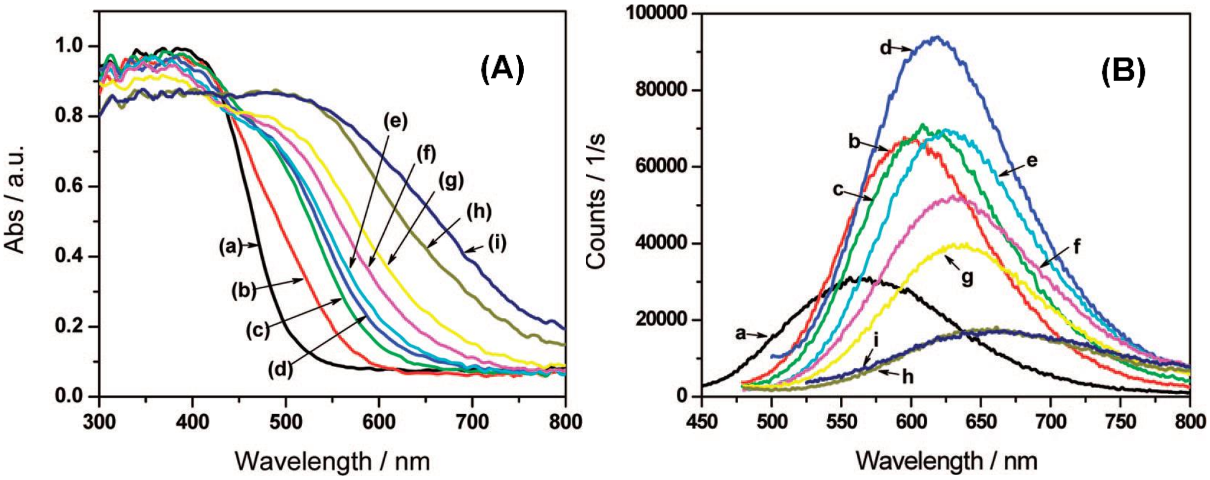

Figure 1.7 (A) Diffuse reflectance spectra of Cu(X)-ZnIn2S4; the values of X were (a) 0.0 wt%, (b) 0.1 wt%, (c) 0.3 wt%, (d) 0.5 wt%, (e) 0.7 wt%; (f) 0.9 wt%, (g) 1.2 wt%, (h) 1.6 wt%, (i) 2.0 wt%. (B) Photoluminescence spectra of Cu(X)-ZnIn2S4; the values of X were (a) 0.0 wt%, (b) 0.1 wt%, (c) 0.3 wt%, (d) 0.5 wt%, (e) 0.7 wt%; (f) 0.9 wt%, (g) 1.2 wt%, (h) 1.6 wt%, (i) 2.0 wt%, excited at 330 nm. [47].

According to recent studies, we know that transition metals, rare earth metals and alkaline earth metals have been used in the modification of $ZnIn_2S_4$ photocatalysts. On the one hand, the introduction of certain specific metals can narrow the band gap of $ZnIn_2S_4$ and expand its light absorption range, which is conducive to photocatalytic performance. On the other hand, it can be used as an electron trap to have a positive impact on the structure and morphology, and to a certain extent improve the photocatalytic activity. At the same time, there are still some defects in metal doping. When the content of doping ions exceeds a certain dose, the doping ions can act as recombination sites for photogenerated electrons and holes. Non-metal doping has been studied and proved to be beneficial to photocatalytic performance. Due to its unique application prospects, future research should receive more attention.

1.3.5 Co-catalyst modification of $ZnIn_2S_4$

Modification of $ZnIn_2S_4$ by co-catalyst or construction of heterojunction can expand the light absorption range of $ZnIn_2S_4$, accelerate charge transfer, and make $ZnIn_2S_4$-based composite materials have better photocatalytic performance. In general, the synergistic promoter can comprehensively improve the photocatalytic performance, including activity, selectivity and stability. Precious metals (Pt), transition metal sulfides or oxides (MoS_2, NiS, CdS, PdS, etc.) and some metal-free materials (graphene) can be used as co-catalysts to make $ZnIn_2S_4$ obtain higher photocatalytic activity. At present, the use of promoters to modify $ZnIn_2S_4$ has been extensively studied.

The precious metal platinum is the most commonly used cocatalyst for $ZnIn_2S_4$ catalytic water reduction. Platinum has excellent electrical conductivity and can provide more active sites. Shen et al. compared the photocatalytic activity of Pt-supported $ZnIn_2S_4$ and pure phase $ZnIn_2S_4$ [51]. Using 1.8 mmol CTAB as raw material, after 1 h hydrothermal treatment, spherical $ZnIn_2S_4$-1.8-1 was prepared, which was compared with platinum-loaded $ZnIn_2S_4$-1.8-1. The results show that $ZnIn_2S_4$-1.8-1 loaded with 1.0wt% platinum has the best photocatalytic activity, which is 11 times that of pure phase $ZnIn_2S_4$-1.8-1. If the platinum content is further increased to 3.0wt%, the photocatalytic activity will decrease. The reason for the decrease is the shielding effect and the excessive loading of platinum. The overloaded Pt can provide more recombination sites for light-excited charges. In addition, the optimal loading of platinum for $ZnIn_2S_4$ synthesized by different routes is also different.

However, the scarcity and cost of platinum limit its wide application. MoS_2 is a transition metal sulfide with high anisotropy and two-dimensional layered structure [57], and it is an efficient co-catalyst. For example, Chen et al. used a simple in-situ photo-assisted deposition process to support MoS_2 on $ZnIn_2S_4$ microspheres, and by supporting MoS_2 as a co-catalyst [58], the photocatalytic activity was significantly enhanced. They deposited platinum on $ZnIn_2S_4$ as a parallel experiment. The results showed that the highest hydrogen evolution rate of 0.375wt% $MoS_2/ZnIn_2S_4$ was 8.047 mmol/g·h, while the highest hydrogen evolution rate of pure $ZnIn_2S_4$ was 0.283 mmol/g·h. In contrast, platinum-loaded $ZnIn_2S_4$ showed a hydrogen evolution rate of 5.117mmol/g·h, indicating that $MoS_2/ZnIn_2S_4$ has higher photocatalytic activity. The deposition of MoS_2 inhibited the recombination of electrons and holes on the surface of $ZnIn_2S_4$ and improved the photocatalytic activity. Recently, other transition metal sulfides have been used as promoters to modify $ZnIn_2S_4$. For example, Wei et al. proposed that NiS is an effective co-catalyst, and the combination with $ZnIn_2S_4$ is beneficial to charge transfer and separation of charge carriers [59]. Yu et al. proposed that PdS can act as a co-catalyst [60]. The photocatalytic activity of the PdS-loaded $ZnIn_2S_4/CdIn_2S_4$ composite photocatalyst is 1.6 times that of the $ZnIn_2S_4$ composite photocatalyst.

Graphene has the advantages of large specific surface area, high conductivity, good stability, and adjustable surface properties. It is an effective co-catalyst for photocatalytic hydrogen evolution. Ye et al. synthesized $RGO/ZnIn_2S_4$ composites by simultaneously growing $ZnIn_2S_4$ nanosheets on RGO by a simple one-pot solvothermal method [61]. It is observed that the hydrogen evolution rate of 1.0 wt% $RGO/ZnIn_2S_4$ is the highest, which is 4.3 times that of pure $ZnIn_2S_4$. RGO is a good electron acceptor and mediator. Since the electrons on the CB of $ZnIn_2S_4$ will be transferred to the RGO, a high separation efficiency of photocharges is achieved. In addition to graphene, carbon materials such as carbon quantum dots (CQD) and carbon nanotubes (CNTs) are also used to modify $ZnIn_2S_4$. Chai et al. prepared a composite composite of multi-walled carbon nanotubes and $ZnIn_2S_4$ by hydrothermal synthesis [62]. The $MWCNTs/ZnIn_2S_4$ composite showed the best photocatalytic activity when the hydrogen production rate was 6840 umol/g·h, which was 1.5 times that of pure $ZnIn_2S_4$. A two-step method was used to synthesize a layered core-shell structured carbon nanofiber (CNF) and $ZnIn_2S_4$ composite material [63], and the maximum hydrogen evolution rate achieved was 3.9 times that of pure $ZnIn_2S_4$. In addition to the layered core-shell structure, the modification of carbon nanofibers enables a high separation rate of photogenerated carriers and a wider light absorption range, which improves the photocatalytic activity.

Understand the cocatalyst modified $ZnIn_2S_4$ photocatalyst and its photocatalytic hydrogen release performance. The precious metal platinum is a widely used co-catalyst. Because its lowest Fermin energy level can be used as a trap for trapping electrons, it can significantly improve the photocatalytic performance. However, due to the lack of platinum and its high price, it is necessary to find alternatives to platinum. Therefore, the introduction of transition metal sulfides (such as MoS_2 and NiS) and carbon materials (such as graphene and carbon nanotubes) to modify $ZnIn_2S_4$ significantly improves its photocatalytic activity. Compared with the precious metal platinum, transition metal sulfides and carbon materials are low in cost and large in quantity. For co-catalyst modification, determining the optimal co-catalyst concentration is the key to prevent the photocatalyst from reducing its adsorption capacity and as a photo-generated carrier recombination site.

1.3.6 Heterojunction structure of $ZnIn_2S_4$

A heterojunction is defined as the interface between different semiconductors with different energy band structures, which may lead to energy band alignment. Based on the intrinsic potential gradient between semiconductor heterojunctions, the transmission of electrons is accelerated and the recombination rate of photo-generated carriers is reduced [64-67]. Therefore, many research groups have proposed to build a heterojunction between $ZnIn_2S_4$ and other semiconductors to improve its hydrogen production performance. For example, Mei et al. prepared $In_2S_3/ZnIn_2S_4$ heterojunction photocatalyst, and the hydrogen evolution rate reached 678 μmol/g·h, which was higher than the pure phase In_2S_3 and $ZnIn_2S_4$ [64]. In addition, Yu et al. prepared $ZnIn_2S_4/CdIn_2S_4$ composite photocatalyst by hydrothermal method [60] and found that the hydrogen evolution rate of $ZnIn_2S_4/CdIn_2S_4$ composite photocatalyst was about 2.5 times that of $ZnIn_2S_4$. It is proved that the heterojunction effectively accelerates the electron transfer, thereby improving the photocatalytic activity.

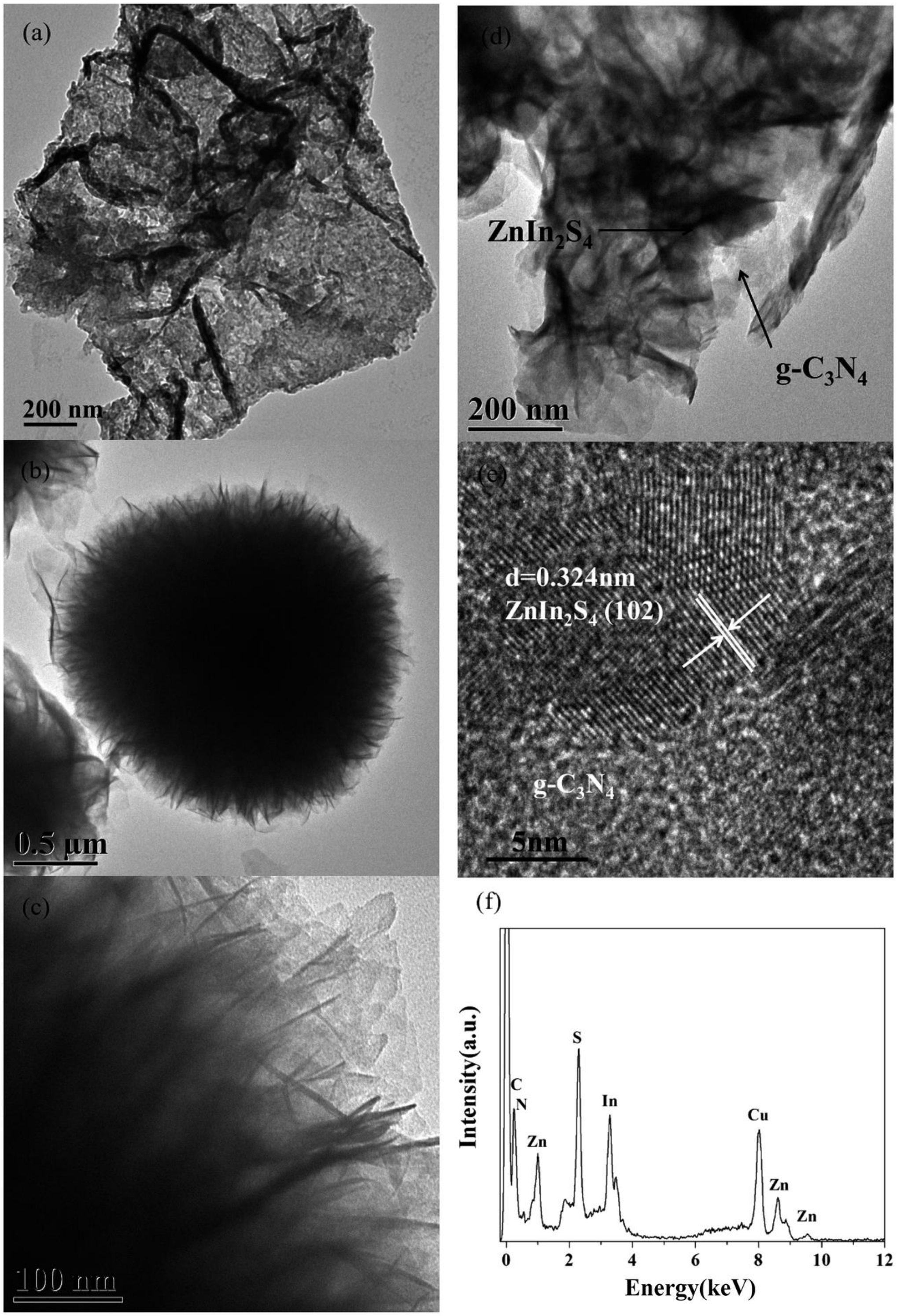

Figure 1.8 TEM images of (a) g-C_3N_4 nanosheets, (b and c) $ZnIn_2S_4$ and (d) ZISCN40, (e) HRTEM image and (f) EDS spectrum of ZISCN40 [68].

In addition to the formation of heterojunctions between two different semiconductors, photocatalysts with ternary heterostructures have also been studied. For example, Chen et al. constructed a $CdS/ZnFe_2O_4/ZnIn_2S_4$ ternary heterostructure composite material through two continuous solvothermal processes and an ion-layer adsorption-reaction method [65]. CdS quantum dots and $ZnFe_2O_4$ nanoparticles were prepared on the $ZnIn_2S_4$ nanosheet three-dimensional film. The results show that $CdS/ZnFe_2O_4/ZnIn_2S_4$ has the highest photocatalytic hydrogen release activity, which is more than three times that of pure $ZnIn_2S_4$. On the one hand, CdS quantum dots and $ZnFe_2O_4$ nanoparticles can be used as photosensitizers to improve light absorption. On the other hand, the unique three-dimensional network porous structure provides more catalytically active sites, increases the contact area between the composite membrane and the reaction solution, thereby promoting the photocatalytic process. Therefore, the interfacial electron migration in the heterojunction leads to a higher separation rate of photogenerated electron-hole pairs and enhanced photocatalytic activity.

Although metal-based semiconductors have been extensively explored and studied, the new type of metal-free semiconductor $g\text{-}C_3N_4$ has attracted widespread attention due to its excellent optical properties and excellent thermochemical stability [66]. In order to increase the hydrogen evolution rate of $ZnIn_2S_4$, $g\text{-}C_3Na_4$ and $ZnIn_2S_4$ are used to form a heterojunction composite material. Liu et al. prepared $ZnIn_2S_4\text{-}g\text{-}C_3N_4$ nanocomposites on a hydrothermal method, as shown in Figure 1.8, and studied the photocatalytic properties of nanocomposites loaded with different $g\text{-}C_3N_4$ contents [68]. As shown in Figure 1.9A, $ZnIn_2S_4$ loaded with 40wt% $g\text{-}C_3N_4$ has the best photocatalytic activity. Due to the low recombination efficiency of photogenerated electron-hole pairs, the promotion effect is obvious. Figure 1.9B shows the possible electron and hole transfer pathways in the formation of a heterojunction. Because the CB edge potential of $g\text{-}C_3N_4$ is more negative, the photogenerated electrons on $g\text{-}C_3N_4$ migrate directly to the CB of $ZnIn_2S_4$. The photo-generated holes on the VB of $ZnIn_2S_4$ migrate to the VB of $g\text{-}C_3N_4$ due to the positive VB potential of $ZnIn_2S_4$. Therefore, the opposing movement directions of photogenerated electrons and holes result in high charge separation efficiency. In addition, Lin et al. synthesized 2D/2D$g\text{-}C_3N_4$ nanosheet@$ZnIn_2S_4$ nanosheet composite material and obtained the best hydrogen production efficiency [68]. 2D/2D$g\text{-}C_3N_4$

nanosheets@$ZnIn_2S_4$ nanosheet composites form face-to-face heterojunctions in the work. With the help of face-to-face heterojunctions, there are many tight high-speed charge transfer nanochannels in the interface junctions. On the one hand, the formed heterojunction leads to a higher separation efficiency of photoelectrons and holes. On the other hand, a large number of charge transfer nanochannels endows high charge carrier transfer efficiency. Thereby achieving excellent photocatalytic performance.

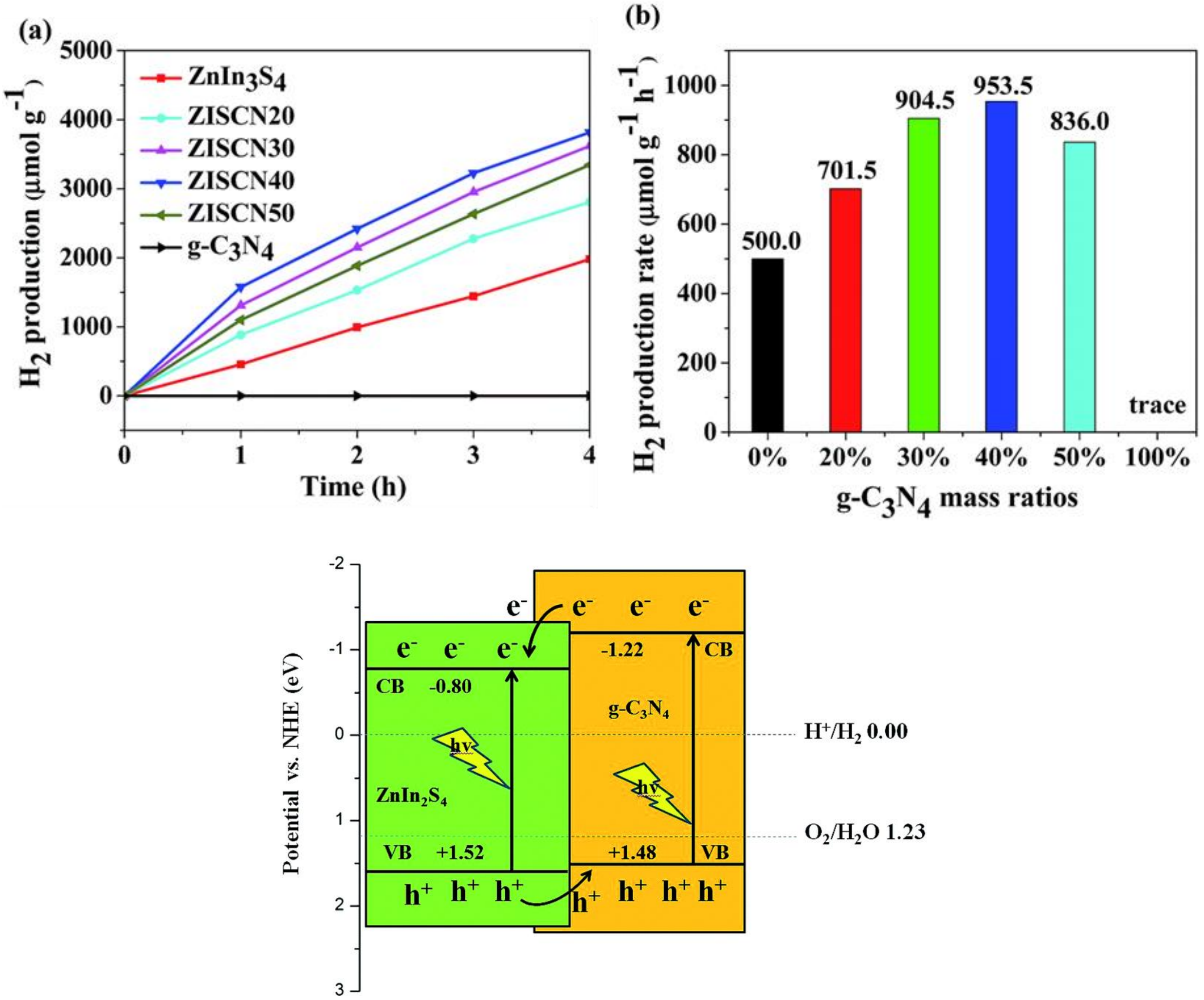

Figure 1.9 (A) (a) Plots of photocatalytic H_2 evolution amount *vs.* irradiation time and (b) comparison of H_2 evolution rate for g-C_3N_4 nanosheets, $ZnIn_2S_4$ and $ZnIn_2S_4$–g-C_3N_4 composites under visible-light irradiation. (B) Mechanism for the enhanced photocatalytic activity of $ZnIn_2S_4$–g-C_3N_4 composites [68].

Therefore, building a heterojunction between $ZnIn_2S_4$ and other semiconductors is an effective and common method to improve the performance of photocatalytic hydrogen evolution. In general, due to the intrinsic potential gradient between semiconductor heterojunctions, photocharge carriers can be effectively separated. Thereby prolonging the life of carriers, which is conducive to the improvement of photocatalytic performance. In addition, depending on the energy band structure between semiconductors, several types of heterojunctions can be formed. Based on the diversity of heterojunctions and semiconductors, the construction of heterojunctions to improve photocatalytic performance has shown great research potential and value.

2 SYNTHESIS METHODOLOGY OF PHOTOCATALYSTS

This work mainly consists of two parts and the first part is the exploration of TiO_2-NFt mass-production methodology. Because the TiO_2 NFts are produced by hydrolysis of potassium titanium oxide oxalate dihydrate ($K_2TiO(C_2O_4)_2·2H_2O$, PTO) in the presence of the additive sodium hypophosphite monohydrate ($NaH_2PO_2·H_2O$, SHP) as a structure-directing agent and the DEG/H_2O binary solvent at 180 °C under solvothermal conditions, the reaction rate of hydrolysis of PTO directly affects the product morphology, meaning the direct effects being from the ratio of PTO/SHP.

Based on the optimized TiO_2 NFts, the ZIS-TiO_2 NFts photocatalysts with a high catalytic ability on the degradation of MO were developed, which were synthesized by in-situ growth on TiO_2 NFts with a $ZnIn_2S_4$ mass fraction of 50 wt% under the hydrothermal condition. And under identical conditions, pure $ZnIn_2S_4$ and $ZnIn_2S_4$-P25 with commercial P25 as the support were prepared to explore the law of the photodegradability of $ZnIn_2S_4$-TiO_2 NFts.

2.1 Materials

Potassium titanium oxide oxalate dihydrate ($K_2TiO(C_2O_4)_2·2H_2O$, ≥98% Ti basis, PTO), sodium hypophosphite monohydrate ($NaH_2PO_2·H_2O$, 99%, SHP), diethylene glycol ($(HOCH_2CH_2)_2O$, 99%, DEG), zinc acetate dihydrate ($Zn(C_2H_3O_2)_2·2H_2O$, ≥98%, $Zn(OAc)_2·2H_2O$), indium acetate ($In(C_2H_3O_2)_3$, 99.99%, $In(OAc)_3$), and thioacetamide (CH_3CSNH_2, 98%, TAA) were used as received from Sigma-Aldrich. All reagents were used without any further purification. Deionized water (resistivity >18 MΩ·cm) produced with a Milli-Q purification system was used to prepare all solutions.

2.2 Production of TiO_2 nanoforests

TiO_2 nanoforests (TiO_2 NFts) can be prepared by a solvothermal approach, which is the hydrolysis of potassium titanium oxide oxalate dihydrate (PTO) under the effect of sodium hypophosphite monohydrate (SHP) as the structure-directed agent in a mixed solvent containing diethylene glycol (DEG) and water. In a representative synthesis, 10.0 ml of water was added to 30.0 ml of DEG and then ultrasonic until being a colorless transparent liquid without any bubbles. Next, 170 mg of SHP was dissolved in the mixed solvent toward a clear solution. Subsequently, 312 mg of PTO was quickly poured into the as-obtained solution in a 50 ml centrifuge tube and immediately shaken with high frequency for 1 min. Afterward, the mixture was transferred to two 40 ml Teflon-lined steel autoclaves and sonicated for 5 min and vigorously stirred by a magnetic stirrer at room temperature for 20 min. Then, the autoclave kept in an oven at 180 °C for 12 h and subsequently cooled naturally to precipitate the product. Finally, the supernatant was discarded and the white precipitate was collected and washed with hot water (80 °C) and isopropanol alternately by centrifugation with a speed-of-rotation range from 5000 to 8000 rpm for 10 min. The purified products were dried at 80 °C overnight to obtain the TiO_2 NFts.

2.3 **Preparation of $ZnIn_2S_4$ photocatalysts**

The $ZnIn_2S_4$ photocatalysts were prepared by a hydrothermal approach in a aqueous solution containing $Zn(OAc)_2$, $In(OAc)_3$ and TAA with the molar ratio of 1:2:4. Typically, 220 mg of $Zn(OAc)\cdot 2H_2O$ (1 mmol), 580 mg of $In(OAc)_3$ (2 mmol) and TAA (4 mmol) were dissolved in 100 mL of water to acquire a $ZnIn_2S_4$ precursor solution. Afterward, the solution was transferred to Teflon-lined steel autoclaves and kept in an oven at 160 °C for 6 h and subsequently cooled down to room temperature. After the yellow precipitate was collected by centrifugation and washed several times with ethanol and water and dried at 80 °C overnight, $ZnIn_2S_4$ photocatalysts were obtained.

2.4 **Synthesis of hybrid $ZnIn_2S_4$-TiO_2 nanoforest photocatalyst**

The hybrid $ZnIn_2S_4$-TiO_2 nanoforest ($ZnIn_2S_4$-TiO_2 NFt) was prepared by $ZnIn_2S_4$ in-situ grown on TiO_2 nanoforest under hydrothermal. For representative 50 wt% $ZnIn_2S_4$-TiO_2 NFts, 100 mg of TiO_2 NFts were dispersed in 23.6 mL $ZnIn_2S_4$ precursor solution with vigorously stirring by a magnetic stirrer at room temperature for 10 min. Subsequently, the mixture was transferred to Teflon-lined steel autoclaves and kept in an oven at 160

°C for 6 h. The yellow precipitate was collected by centrifugation and washed several times with ethanol and water and dried at 80 °C overnight to obtain $ZnIn_2S_4$-TiO_2 NFt photocatalysts.

For the preparation of a hybrid photocatalyst for comparison, $ZnIn_2S_4$-P25, the synthetic procedures were similar to that of $ZnIn_2S_4$-TiO_2 NFts except that commercial P25 is used instead of TiO_2 NFts.

2.5 Manufacture of mixture photocatalysts for comparison

To more clearly exhibit the structural characteristics and photocatalytic performance of the hybrid $ZnIn_2S_4$-TiO_2 NFt, a mixture photocatalyst, denoted as $ZnIn_2S_4$+TiO_2 nanoforest, was manufactured. In a typical experiment, 100 mg of $ZnIn_2S_4$ powder and 100 mg of TiO_2 NFts powder were thoroughly mixed to obtain this product.

2.6 Materials characterization

The field-emission scanning electron microscopy (FESEM, JSM-6700F, JEOL) and high-resolution analytical transmission electron microscopy (HRTEM, JEM-2100F, JEOL, at an accelerating voltage of 200 kV) were employed to observe the morphology and structure of as-prepared nanoforests.

The X-ray diffraction (XRD) patterns were obtained on a D/max-γA X-ray diffractometer (Rigaku, Japan), operated at 40 kV and 70 mA, using Cu Kα radiation ($\lambda = 0.154178$ nm) and at a scanning ratio of 10° min in 2θ ranging from 10° to 80°.

The UV−vis−NIR absorption spectra of samples and the absorbance of MO in aqueous solutions were measured using a Varian Cary 5000 scan spectrometer.

The upconversion luminescence spectra were obtained by using a Thorlabs fiber-coupled laser diode (maximum power: 330 mW) as the 980 nm excitation light source. The laser was focused on the powder to obtain a spot (0.4 mm in diameter) with a Gaussian distribution of intensity. The emission was collected at 90° from the incident beam and then transferred and recorded on a spectrophotometer (Avaspec-2048L-USB2).

All the measurements were performed under ambient conditions.

2.7 **Photocatalytic performance evaluation**

The evaluation of photocatalytic performances of the $ZnIn_2S_4$-TiO_2 photocatalysts was carried out in the photodegradation of MO. In a typical experiment, 10 mg of the measured photocatalyst was dispersed into 25 mL of MO solution (30 mgL^{-1}) in a 100 mL quartz reactor with circulating cooling water to keep the reaction temperature constant. Prior to illumination, the mixed suspension was magnetically stirred in the dark for 30 min to obtain the adsorption−desorption equilibrium. The UV photocatalysis experiment was performed using a commercial photoreactor (LUZ-4 V, Luzchem), which was equipped with fourteen 8W UV lamps (Luzchem LZC-UVA). Visible light with different wavelengths, $\lambda > 420$ nm and solar spectrum, was generated by applying appropriate long-pass optical filters onto a 300 W xenon lamp. A 980 nm diode laser was set at 2 W to work as the NIR light source. After irradiation for various time intervals, 0.8 mL of MO solution was collected and centrifuged. The absorbance of MO in the supernatant was analyzed by UV−vis absorption spectrometry. Also, to study the MO degradation kinetics in the presence photocatalysts, the apparent reaction rate constant (k) was calculated by using the following first-order reaction model:

$$\ln\frac{c_0}{c} = kt$$

where c_0 is the MO concentrations at time 0

c is the MO concentrations at time t

The normalized reaction rate constant was calculated by normalizing k with the total mass of catalysts.

3 ZINC INDIUM SULFIDE - TITANIUM DIOXIDE NANOFOREST HYBRID PHOTOCATALYSTS

3.1 Introduction

In early 1972, Fujishima and Honda discovered that under the irradiation of ultraviolet light, H_2 could be separated out by photoelectrochemical decomposition of wate [24]. Inspired by his pioneering work, semiconductor photocatalysis technology has been widely used in water splitting and other fields, such as CO_2 reduction, decontamination, bacterial disinfection, and selective synthesis of organic compounds. However, the classical TiO_2 nanocatalysts are often constrained by the problems of limited light absorption, inefficient charge transfer, and significant charge recombination,etc.,and cannot achieve effective environmental remediation [10-12]. Numerous research results show that the size, crystallinity, specific surface area, morphology, and decoration of TiO_2 nanomaterials are considerable influences that impact their performances [11, 12]. To overcome these challenges for practical application, the hierarchical structure was proposed as a potential solution.

In the term of hierarchically structured TiO_2, three-dimensional nanoforests used to be an exciting development in material science [13-16]. In the application on solar cells, Sauvage and co-workers demonstrated a PLD method to fabricate vertically aligned anatase TiO_2-forest arrays directly on FTO glass and use these structures for the photoanode in dye-sensitized solar cells, which achieved 4.9% conversion efficiency in combination with C101 dye [14]. For the energy field, Qin and co-workers successful access to the TiO_2 nano-forest photocatalysts with large-size plasmonic Pt NPs attaching, which exhibit outstanding activity and durability for visible-light-driven water splitting [13]. Distinguished from the more frequently used nanoparticles like nanorods (NRs), nanowires (NWs) and nanotubes (NTs), the hierarchical TiO_2 nanoforests (NFts) are composed of nanowires as branches and nanorods trunks possess an architecture and provide numerous advantages: (i) enlarged surface area for attaching enhanced functional units; (ii) rapid electron transfer in virtue of direct charge transfer pathway in both trunks and branches; (iii) long electron lifetime for efficient charge collection; (iv) diffusion length of charge carriers, increased light trapping and superior multi-scattering capability for enhanced light harvesting; (v) interlaced and intertwined structure for improved reactant diffusion [17-20]. All of the above-mentioned fascinating advantages actuate that TiO_2 NFts have been successfully incorporated into various photocatalytic and photovoltaic products and consistently demonstrate markedly improved performance. Therefore, TiO_2 NFts offer a feasible strategy for environmental applications.

3.2 Structural and morphological characterization

3.2.1 Structural and morphological characterization of TiO_2 NFts

Figure 3.1 presents the results of structural and morphological characterization for TiO_2 NFts. From the SEM images (Figure 3.1a, b, and c), the structural features of TiO_2 NFts is that high-dense TiO_2 nanowires are grown outward from the whole primary TiO_2 trunk with a length of 1-2 μm. Also, the sample can be observed to be uniform in morphology. In the TEM images (Figure 3.1d, e), the ultrafined branches can be observed more clearly and the measured d spacing of ~0.35, ~0.37 and ~0.38 nm can be indexed to the lattice spacing of the (101) plane of anatase. Corresponds to the set of diffraction rings indexed to anatase in the selected area electron diffraction (SAED) pattern (Figure 3.1f), it is determined that the component of TiO_2 NFts contains the anatase only, in good agreement with those results in the literature [13-16].

In order to further determine the composition and purity of the prepared catalysts, the TiO_2 NFts sample was characterized by XRD and XPS (Figure 3.2). From Figure 3.2a, the diffraction peaks indexed to the anatase phase of TiO_2 (JCPDS 21-1272) are clearly observed for TiO_2 NFts. The above results indicate that TiO_2 NFts are monophase anatase and feature high crystallinity. XPS measurement is performed to study the oxidation states of Ti and O in these samples. As shown in Figure 2b, the two peaks of Ti $2p_{3/2}$ and Ti $2p_{1/2}$ are assigned to Ti(IV) components, indicating that the Ti(IV) is the dominant oxidation state in these samples. For O 1s spectra (Figure 2c), it can be fitted with three peaks. One is centered at ~530 eV, characteristic of lattice oxygen (denoted as Ti-O-Ti) and the second one located at ~532.7 eV is indexed to surface oxygen (denoted as Ti-OH), and the weakest peak is located at ~527.8 eV, which is accepted as impurity species of $C_2O_4^{2-}$ from PTO. Obviously, the area of surface oxygen peak in the TiO_2 NFts is stronger than commercial P25, corresponding to the structural features of TiO_2 NFts, implying more surface-active sites provided by its branches, which creates an advantageous environment for the electron transmission and charge separation of $ZnIn_2S_4$ modified TiO_2 NFts.

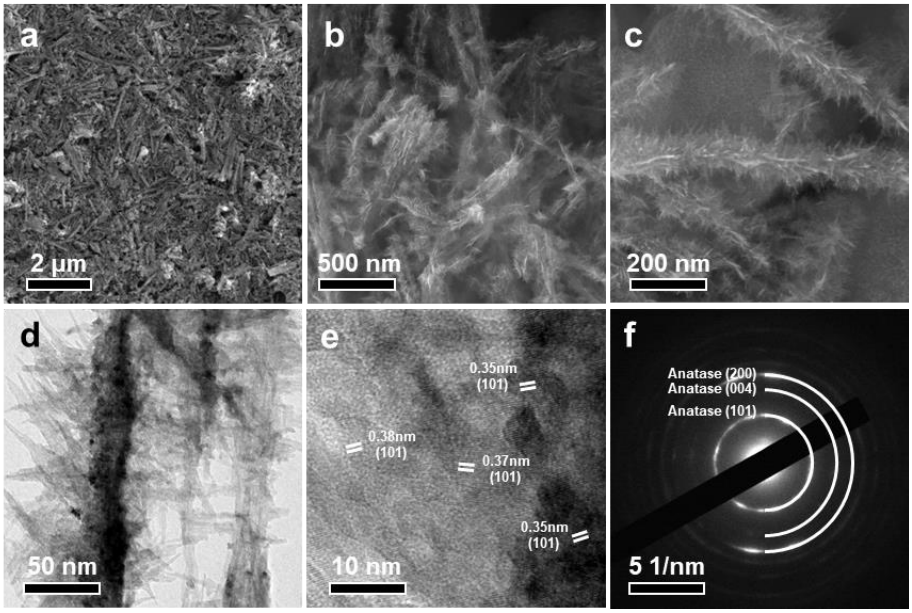

Figure 3.1 SEM images (a-c), TEM images (d, e) and SAED pattern (f) of TiO_2 NFts.

The ultrafined TiO_2 nanowires provide a high specific surface area for attaching $ZnIn_2S_4$ and harvesting light, close contact for carrier migration, and more active sites with pollutants, while the large central trunks enhance light scattering. These characteristics of TiO_2 NFts result in a considerable extension of the light propagation distance within the ensemble of the TiO_2 NFts and thereby increase the probability of photons absorption of TiO_2 NFts. The photocatalytic capability could be greatly promoted by such a synergistic interaction of the different parts of TiO_2 NFts. These advantages are reflected in the greatly enhanced degradation performance of the $ZnIn_2S_4$-TiO_2 NFts photocatalyst mentioned later.

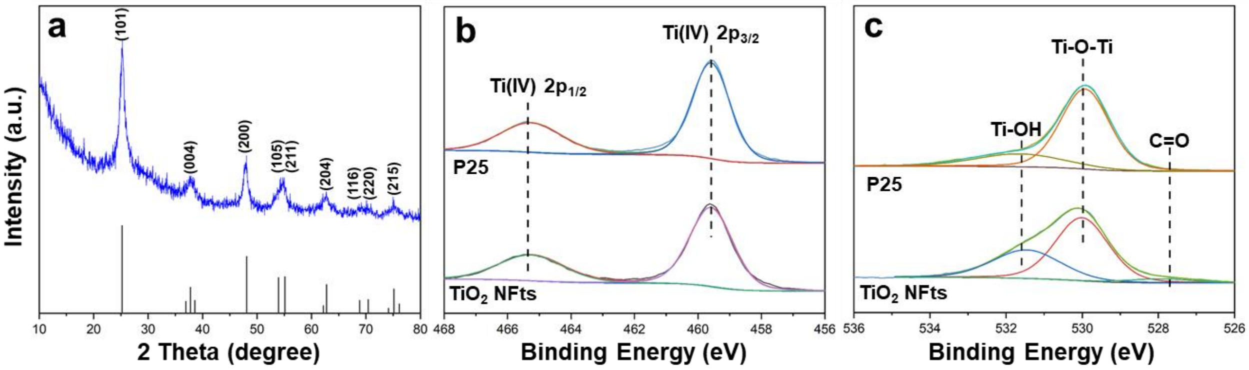

Figure 3.2 XRD patterns (a) of TiO_2 NFts and XPS spectra of Ti 2p (b) and O 1s (c) of TiO_2 NFts and commercial P25. Inset in a is the standard XRD powder pattern of anatase (JCPDS 21-1272).

3.2.2 Structural and morphological characterization of $ZnIn_2S_4$-TiO_2 NFts and comparative photocatalysts

Structural features of the $ZnIn_2S_4$-TiO_2 NFts and comparative photocatalysts are examined by XRD (as shown in Figure 3.3). The diffraction peaks indexed to the anatase phase of TiO_2 (JCPDS 21-1272) corresponded to the crystallographic features of TiO_2 NFts, can be observed in the patterns of hybrid $ZnIn_2S_4$-TiO_2 NFts, and the mixture of $ZnIn_2S_4$ and TiO_2 NFts. For the $ZnIn_2S_4$, two sets of prominent peaks are exhibited, where the peaks at 14.4°, 27.8°, 33.7°, and 48.4° assigned to the (111), (311), (400), and (440) planes of cubic $ZnIn_2S_4$ (JCPDS 48-1778) and the peaks at 21.6°, 27.7°, and 30.4° corresponds to the (006), (102), and (104) planes hexagonal $ZnIn_2S_4$ (JCPDS 65-2023), suggesting the formation of hexagonal phase and coexistence of two different phases in $ZnIn_2S_4$-based photocatalysts, which presents the possibility of generating a homojunction by the cubic and hexagonal $ZnIn_2S_4$. It will allow TiO_2 NFts to combine with the hexagonal $ZnIn_2S_4$ to overcome its carrier recombination and further improve the photodegradation performance via the combination of TiO_2 NFts and homojunction $ZnIn_2S_4$.

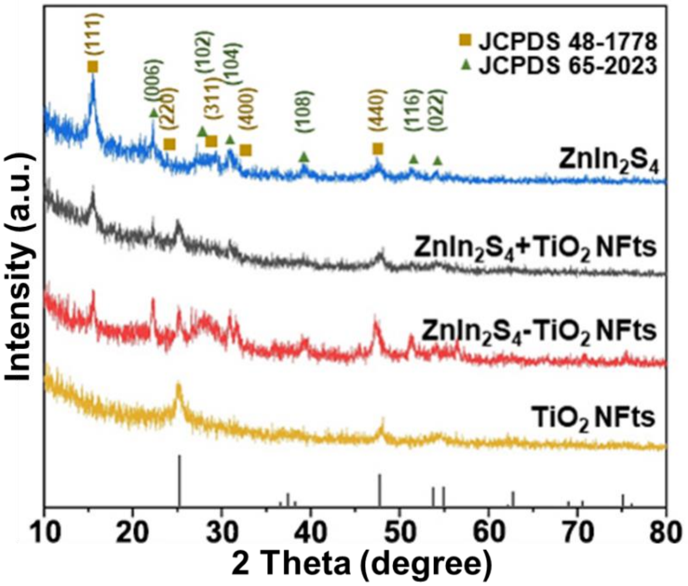

Figure 3.3 XRD patterns of $ZnIn_2S_4$, TiO_2 NFt, hybrid $ZnIn_2S_4$-TiO_2 NFt and mixture of $ZnIn_2S_4$ and TiO_2 NFt photocatalysts. The inset is the standard XRD powder pattern of anatase (JCPDS 21-1272).

The morphology and structure of $ZnIn_2S_4$-TiO_2 NFt photocatalyst was thoroughly investigated by various techniques (Figure 3.4). As shown in Figure 3.4a, b, the $ZnIn_2S_4$ is compounded with the TiO_2 NFt and clearly distinguished between two kinds of particles with individual morphologies including thin nanosheets and nanocubes. With further exploration by high-resolution TEM images (Figure 3.4d, e), the measured d spacing ~0.31 nm, ~0.32 nm and ~0.33 nm can be indexed to the lattice spacing of the (102) and (100) plane of hexagonal $ZnIn_2S_4$, and ~0.38 nm can be indexed to that of cubic $ZnIn_2S_4$. Notablely, A set of characteristic angle of (100) planes of hexagonal lattices can be observed, which further illustrates the existence of hexagonal $ZnIn_2S_4$. Meanwhile, the SAED pattern of $ZnIn_2S_4$-TiO_2 NFts clearly exhibits three sets of diffraction rings corresponding to cubic $ZnIn_2S_4$ and hexagonal $ZnIn_2S_4$ and anatase, respectively. These results preliminarily confirmed the three components contained in the as-synthesized $ZnIn_2S_4$-TiO_2 NFts photocatalyst, in good agreement with the analysis of the XRD patterns.

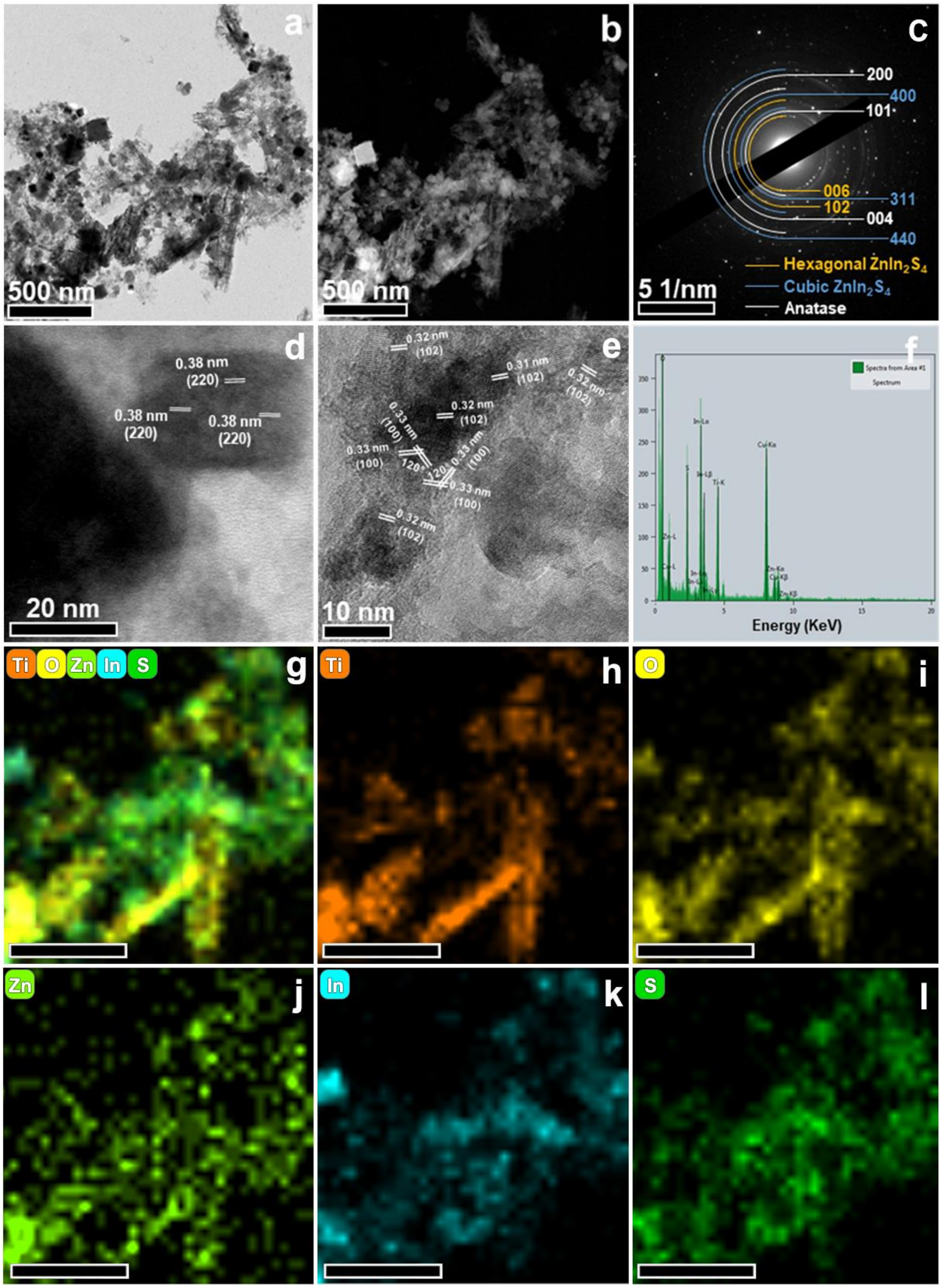

Figure 3.4 TEM images (a, b, d, e), SAED pattern (c), EDS spectra (f) and corresponding elemental mapping (g-l) of $ZnIn_2S_4$-TiO_2 NFt photocatalysts. The bars in (g)-(l) are corresponding the 500 nm.

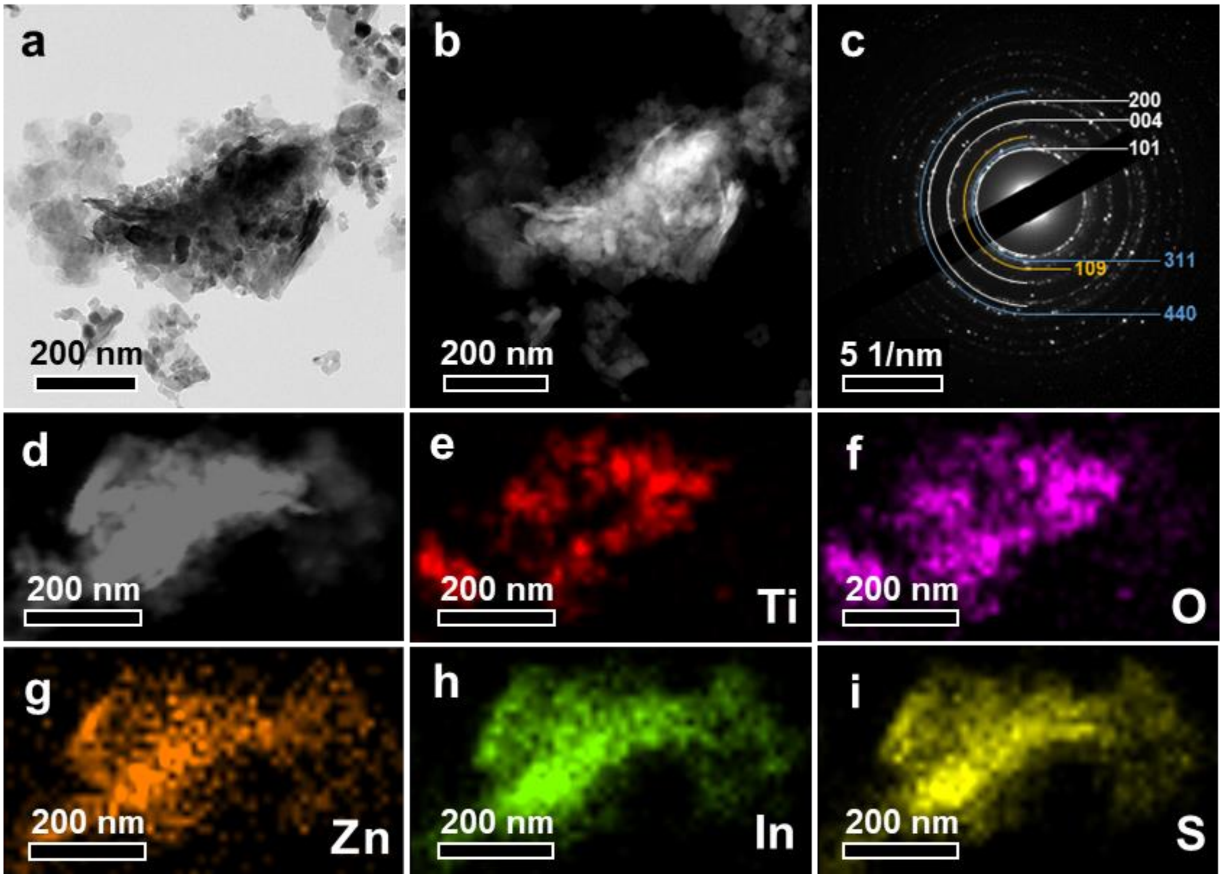

Figure 3.5 TEM images (a, b and d), SAED pattern (c) and corresponding elemental-mapping (d-i) of $ZnIn_2S_4$-P25 photocatalyst. The diffraction rings marked in yellow, blue, and white in c correspond to hexagonal $ZnIn_2S_4$, cubic $ZnIn_2S_4$, and anatase, respectively.

To further investigate the elemental distribution of Ti, O, Zn, In and S, EDS mapping images are shown in Figure 3.4h-l, in which the Zn, In and S are uniformly distributed in the $ZnIn_2S_4$-TiO_2 NFts. For the distribution of the Ti and O, the outlines of TiO_2 NFts are still discernible, which overlap in the region of $ZnIn_2S_4$. Such distribution can be easily seen that the $ZnIn_2S_4$ is composited with TiO_2 NFts to construct a heterojunction, which can facilitate the transmission of carriers and the utilization of the light by all components. Also, it indicates that the TiO_2 NFts serve as the support of $ZnIn_2S_4$, and they are capable of retaining their initial crystal characteristics when introducing these components. The $ZnIn_2S_4$-P25 photocatalyst was a comparative sample for $ZnIn_2S_4$-TiO_2 NFts.

The morphology and structure of $ZnIn_2S_4$-P25 was investigated by TEM and SAED (Figure 3.5). As shown in Figure 3.5a and b, the $ZnIn_2S_4$ is also compounded with the P25. Also, the SAED pattern of $ZnIn_2S_4$-TiO_2 NFts clearly exhibits three sets of diffraction rings corresponding to cubic $ZnIn_2S_4$ and hexagonal $ZnIn_2S_4$ and anatase, respectively. These results preliminarily confirmed the similar components in the as-synthesized $ZnIn_2S_4$-P25 photocatalyst with $ZnIn_2S_4$-TiO_2 NFts. Meanwhile, it verifies that the TiO_2 will not play the role causing changes in the crystal structure and morphology for the synthesize of $ZnIn_2S_4$.

Further investigating the elemental distribution of Ti, O, Zn, In and S, EDS mapping images are shown in Figure 3.5e-i, in which the Zn, In and S are uniformly distributed in the $ZnIn_2S_4$-P25. For the distribution of the Ti and O, P25 overlaps in the region of $ZnIn_2S_4$. Such distribution can be easily seen that the $ZnIn_2S_4$ is composited with P25 as a hybrid photocatalyst with the construction consistent with $ZnIn_2S_4$-TiO_2 NFts.

3.3 Optical properties

For the comparison of optical properties, the UV−vis absorption spectra of $ZnIn_2S_4$-TiO_2 NFts, TiO_2 NFts, and $ZnIn_2S_4$ photocatalysts were recorded as presented in Figure 3.6. In the UV-vis region, the typical absorption feature of hexagonal $ZnIn_2S_4$ with an absorption edge at ~500 nm is observed in the samples involving $ZnIn_2S_4$. It corresponds to the electron excitation from the valence band (VB) to the conduction band (CB) of hexagonal $ZnIn_2S_4$ which represents a bandgap energy of ∼2.5 eV. The TiO_2 NFts presents an absorption less than 380 nm, corresponding to the optical properties of anatase which provided a bandgap of ∼3.2 eV and the invalid optical absorption in the region of $\lambda > 420$ nm.

Figure 3.6c shows the steady-state photoluminescence (PL) spectra of $ZnIn_2S_4$-TiO_2, $ZnIn_2S_4$, and TiO_2 samples. The PL quenching in $ZnIn_2S_4$-TiO_2 NFts indicates greatly suppressed recombination, which can be attributed to the efficient interfacial charge transfer from $ZnIn_2S_4$ to TiO_2 NFts. The charge carrier dynamics were investigated by time-resolved PL (TRPL) spectroscopy (Figure 3.6d-f). A biexponential fitting equation was applied to analyze the TRPL decay curves due to their complexity. The decay kinetics of $ZnIn_2S_4$-TiO_2 NFts shows a shorter average PL lifetime (129 ± 5 ns) than those of ZIS (222 ± 4 ns) and TNF (161 ± 2 ns). The decreased PL lifetime in the $ZnIn_2S_4$-TiO_2 NFts heterojunction supports that the introduction of ZIS can effectively facilitate the separation of photogenerated charge carriers.

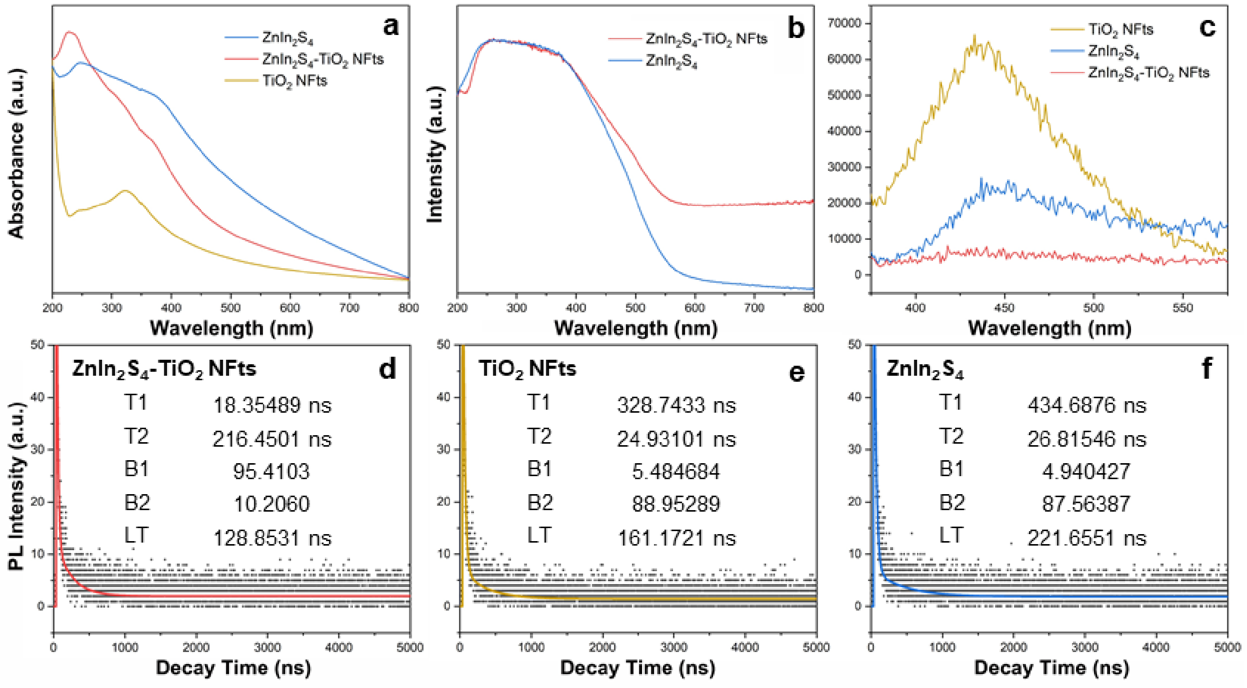

Figure 3.6 UV−vis absorption spectra (a), DRS spectra(b), steady-state PL spectra (c) with the excitation at 375 nm, and TRPL decay curves (d-f) measured at 440 nm of the $ZnIn_2S_4$-TiO_2 NFts, $ZnIn_2S_4$ and TiO_2 NFts.

3.4 Photocatalytic performance

As shown in the absorption spectra of MO over $ZnIn_2S_4$-TiO_2 NFt photocatalysts (Figure 3.4), after reaching the absorption-desorption equilibrium, the intensities of characteristic peak of MO, positioning at ~465 nm, are still relatively high. With the increase of light irradiation time, the intensities steadily decrease, reflecting that MO in solution is degraded gradually.

Figure 3.7 illustrate the rates of photocatalytic degradation of MO from an aqueous solution (25 mL of 30 mg/L MO) for various photocatalysts as a function of time under visible light ($\lambda > 420$ nm) illumination. Under visible light, all other samples exhibit higher photocatalytic activity than the TiO_2 NFts photocatalyst (Figure 3.7a). TiO_2 NFts do not exhibit any activity, indicating that TiO_2 NFts exhibits no optical absorption in the region of $\lambda > 420$ nm. It is a consistent result with those results from the UV−vis absorption spectra and in the literature [13]. All of the samples involving $ZnIn_2S_4$ present a higher rate of degradation of MO than that of pure TiO_2 samples. Therefore, the $ZnIn_2S_4$ appears to further promote photocatalytic activity under visible light illumination. For the photocatalyst of mixture of $ZnIn_2S_4$ and TiO_2 NFts (denoted as $ZnIn_2S_4$+TiO_2 NFts), its performance seems to be almost the same as that of $ZnIn_2S_4$, further confirming that TiO_2 NFts exhibits no response to visible light. Figure 3.7d shows the kinetic study of MO degradation over each photocatalysts. The rate constant calculated from the first-order reaction model follows the order: $ZnIn_2S_4$-TiO_2 NFts > $ZnIn_2S_4$ > $ZnIn_2S_4$-P25 > $ZnIn_2S_4$+P25 > $ZnIn_2S_4$+TiO_2 NFts > P25 > TiO_2 NFt (as shown in Table 3.1). The highest normalized reaction rate constant (12.9×10^{-4} min^{-1} mg^{-1}) achieved by $ZnIn_2S_4$-TiO_2 NFts is 1.3 times higher than that (9.8×10^{-4} min^{-1} mg^{-1}) by $ZnIn_2S_4$.

When the reaction system is exposed to solar light, $ZnIn_2S_4$-TiO_2 NFts still exhibit higher photocatalytic activity than all other photocatalyst (Figure 3.7b). The rate constant calculated from the first-order reaction model follows the order: $ZnIn_2S_4$-TiO_2 NFts > $ZnIn_2S_4$+P25 > $ZnIn_2S_4$ > $ZnIn_2S_4$+TiO_2 NFts > $ZnIn_2S_4$-P25 > P25 > TiO_2 NFt (as shown in Table 3.2). The highest normalized reaction rate constant (19.5×10^{-3} min^{-1} mg^{-1}) achieved by $ZnIn_2S_4$-TiO_2 NFts is 2.5 times higher than that (7.6×10^{-3} min^{-1} mg^{-1}) by $ZnIn_2S_4$ and 2.7 times higher than that (7.0×10^{-3} min^{-1} mg^{-1}) by $ZnIn_2S_4$+TiO_2 NFts. The greatest photocatalytic activity was achieved by the hybrid $ZnIn_2S_4$-TiO_2 NFt photocatalysts, indicating that the mixed-phase $ZnIn_2S_4$ could play an important role in the formation of heterojunction resulting in enhancing photocatalysis far superior to the mixture of $ZnIn_2S_4$ and TiO_2 NFts.

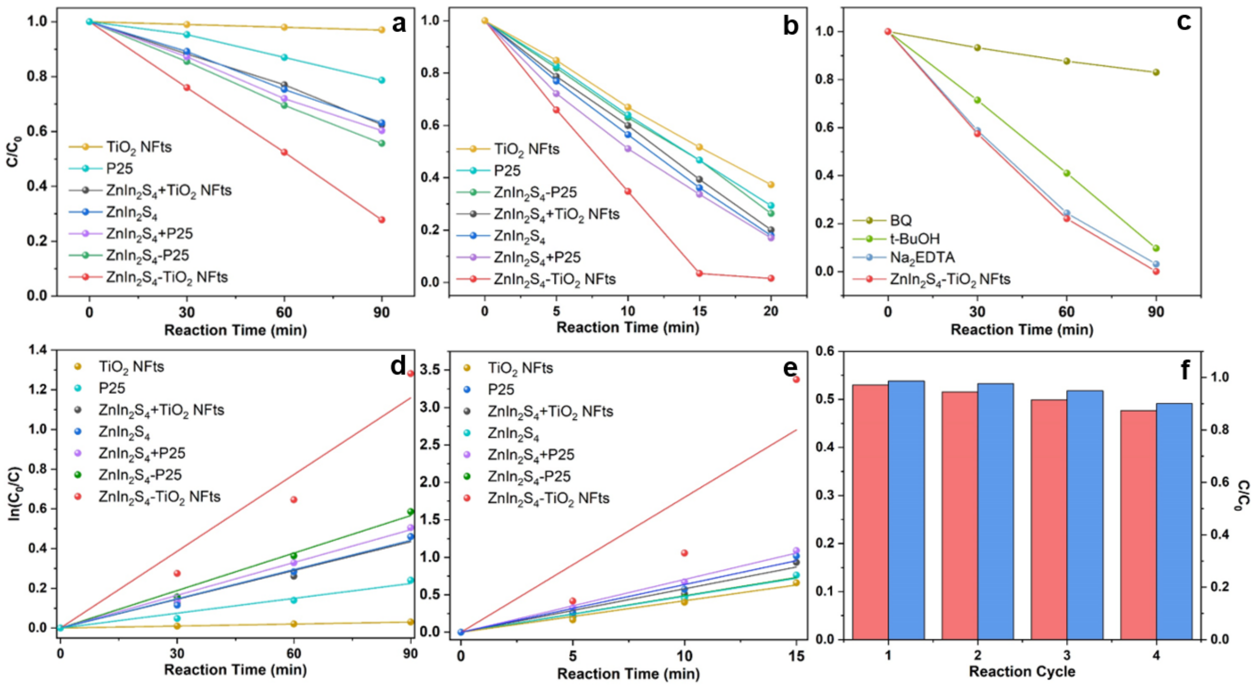

Figure 3.7 The plot (a) and the kinetics study (d) of the time-dependent MO for 10 mg of each photocatalyst in 25 mL of 30 mg/L MO solution degradation under visible irradiation with a 420 nm filter. The plot (b) and the kinetics study (e) of the time-dependent MO for 10 mg of each photocatalyst in 25 mL of 30 mg/L MO solution degradation under solar spectrum. The plot (c) of trapping experiments and histogram (f) of durability measurement for 10 mg $ZnIn_2S_4$-TiO_2 NFts photocatalysts in 25 mL of 30 mg/L MO solution degradation under visible irradiation with a 420 nm filter for 60 min each time and under solar irradiation for 15 min each time.

Table 3.1 Kinetic constants of the obtained samples under visible irradiation.

Sample	$ZnIn_2S_4$-TiO_2 NFts	$ZnIn_2S_4$-P25	$ZnIn_2S_4$+P25
K*10^4 (min^{-1} mg^{-1})	12.9	6.3	5.5
Sample	$ZnIn_2S_4$	$ZnIn_2S_4$+TiO_2 NFts	P25
K*10^4 (min^{-1} mg^{-1})	9.8	4.8	2.5

Table 3.2 Kinetic constants of the obtained samples under solar spectrum.

Sample	$ZnIn_2S_4$-TiO_2 NFts	$ZnIn_2S_4$-P25	$ZnIn_2S_4$+P25
K*10^3 (min^{-1} mg^{-1})	19.5	5.8	8.0
Sample	$ZnIn_2S_4$	$ZnIn_2S_4$+TiO_2 NFts	P25
K*10^3 (min^{-1} mg^{-1})	7.6	7.0	5.5

After conducting four successive runs under visible light and simulated solar light illumination, almost no activity change is found for $ZnIn_2S_4$-TiO_2 NFt photocatalyst, and the performance of degradation of MO still remains more than 85% (Figure 4f). The high performance with the high stability of the as-synthesized photocatalysts under visible light and solar light are beneficial to the large-scale application of photocatalysis in the environmental pollution remediation by using abundant solar energy.

The dramatically increased photocatalytic properties of as-prepared $ZnIn_2S_4$-TiO_2 NFts photocatalysts with respect to the $ZnIn_2S_4$-based and TiO_2-based photocatalysts motivated us to further elucidate the processes involved in the degradation of MO. It is expected that the active species, such as photogenerated holes, superoxide radicals ($\bullet O_2^-$), and hydroxyl radicals (•OH), are likely to be actively involved in the photocatalytic degradation of organic molecules [93, 94]. Accordingly, the trapping experiments in the presence of three different types of scavengers, BQ, t-BuOH, and Na_2EDTA, were designed to identify the active species involved in this reaction system (Figure 3.7c). The slight suppression in the degradation of MO is observed by the addition of the hole scavenger, Na_2EDTA (1 mM). While in the presence of the $\bullet O_2^-$ radical scavenger, BQ (1 mM), and •OH radical scavenger, t-BuOH (1 mM), the photocatalytic reaction were obviously retarded, with the photocatalytic degradation rate being reduced by 18% and 90%, respectively, after 90 min of visible light exposure [95-98]. Apparently, the $\bullet O_2^-$ and •OH radicals play more important roles than the holes in the photocatalytic degradation of MO.

To elucidate whether the interfacial charge transfer between TiO_2 and $ZnIn_2S_4$ complies with the type-II heterojunction pathway, ISI-XPS characterization was performed (Figure 3.8) [99]. Without light irradiation, the $ZnIn_2S_4$-TiO_2 NFts exhibited two peaks at 458.6 (Ti $2p_{3/2}$) and 464.2 eV (Ti $2p_{1/2}$) attributed to TiO_2. Upon light irradiation, there was a slight negative shift (by -0.2 eV) in the Ti 2p binding energy, suggesting a decrease in its electron density under light irradiation. Meanwhile, two characteristic peaks attributed to $ZnIn_2S_4$ at 445.0 (In $3d_{5/2}$) and 452.6 eV (In $3d_{3/2}$) were observed without light, which underwent a positive shift (by 0.2 eV) under light irradiation, suggesting an increase in the electron density on the TiO_2. These binding energy shifts provide direct evidence of the charge carrier migration pathway across the $ZnIn_2S_4$-TiO_2 NFts interface under the same light irradiation condition as the photocatalytic reaction. In detail, the photogenerated electrons migrate from $ZnIn_2S_4$ to TiO_2, which is in good agreement with the type-II mechanism (Figure 3.9).

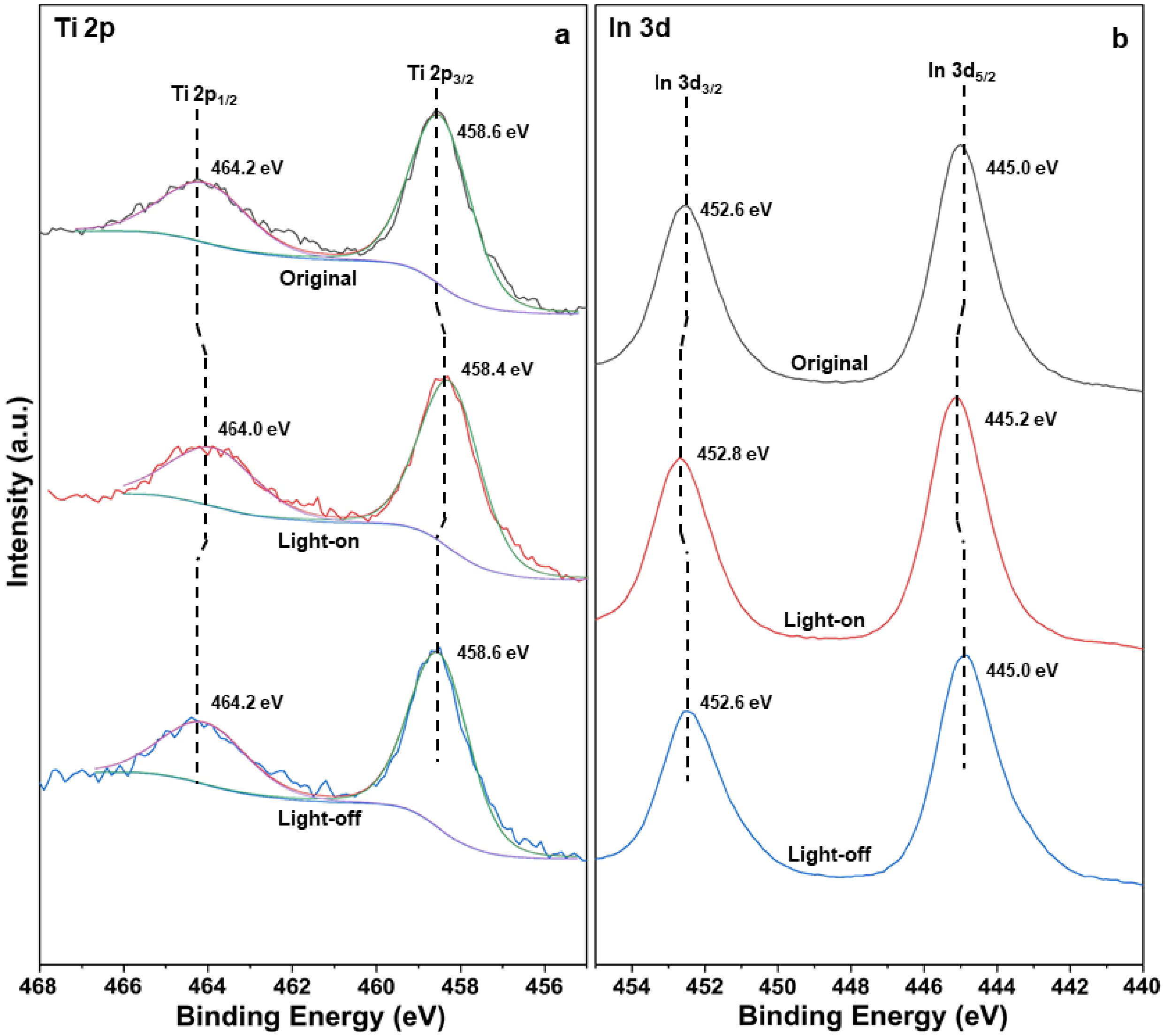

Figure 3.8 High-resolution Ti 2p (a) and In 3d (b) ISI-XPS spectra of $ZnIn_2S_4$-TiO_2 NFts.

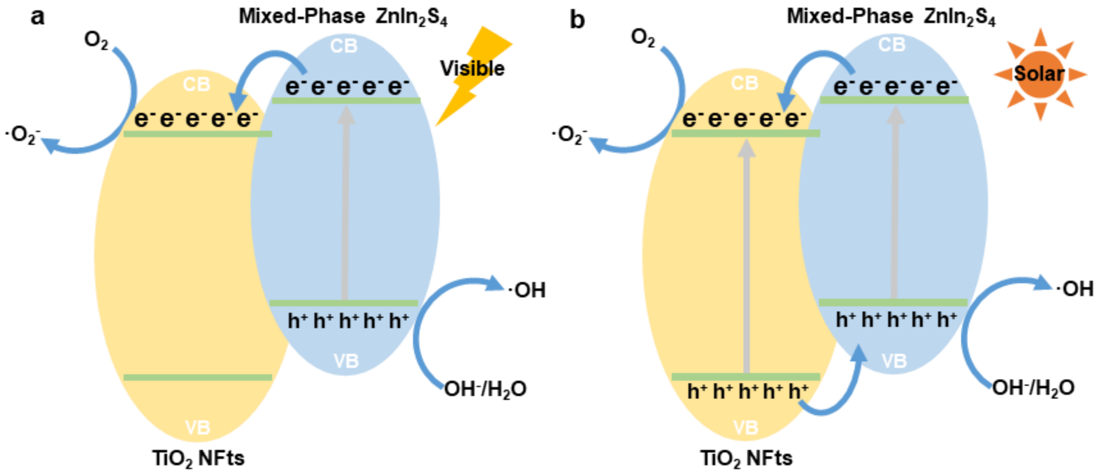

Figure 3.9 Proposed photocatalytic mechanism of $ZnIn_2S_4$-TiO_2 NFt photocatalysts under (a) visible light ($\lambda > 420$ nm) and (b) solar light irradiation, respectively.

In summary, strong evidence based on the ISI-XPS characterization, and trapping experiment confirms the formation of the type-II heterojunction between TiO_2 and $ZnIn_2S_4$. The formation of type-II heterojunction can greatly enhance the utilization of the photogenerated electrons and holes with high reduction and oxidation abilities, respectively. As a result, the photocatalytic MO degradation performance of the $ZnIn_2S_4$-TiO_2 NFts composite was significantly higher than that of $ZnIn_2S_4$, TiO_2 NFts, commercial TiO_2 (P25), and other comparative samples for photodegradation. This work comprehensively confirms the presence of the excellent $ZnIn_2S_4$-TiO_2 NFts through experimental and theoretical analyses, providing important inspiration for future development of semiconductor composites in efficient solar energy utilization, greatly meeting the requirements of the environmental application.

4 CONCLUSION

Utilizing the positive effect of hierarchically structured TiO_2 three-dimensional nanoforests on carrier transfer to overcome the ultrafast carrier recombination of $ZnIn_2S_4$, a greatly broadened light response range, and enhanced photocatalytic activity is obtained. Meanwhile, the combination of hexagonal and cubic phases of $ZnIn_2S_4$ further enhances the light absorption of the photocatalyst. In this work, the $ZnIn_2S_4$-TiO_2 NFts were produced through a simple hydrothermal method. The synthesized photocatalyst showed excellent activity in the photocatalytic degradation of MO. According to the optical properties and photodegradation experiments under different light irradiation, the dynamics were studied. It is found that the rate constant of the obtained photocatalyst is superior to other comparative photocatalysts in the visible light region, while its rate constant is increased to three times that of $ZnIn_2S_4$ under the solar spectrum, which indicates that the developed photocatalyst, $ZnIn_2S_4$-TiO_2, greatly meets the requirements of the environmental application.

5 REFERENCES

[1] Low, J., Yu, J., Jaroniec, M., Wageh, S., & Al-Ghamdi, A. A. (2017). Heterojunction photocatalysts. *Advanced Materials*, 29(20), 1601694.

[2] Liang, Q., Shao, B., Tong, S., Liu, Z., Tang, L., Liu, Y., & Peng, Z. (2020). Recent advances of melamine self-assembled graphitic carbon nitride-based materials: design, synthesis and application in energy and environment. *Chemical Engineering Journal*, 126951.

[3] Cao, S., Low, J., Yu, J., & Jaroniec, M. (2015). Polymeric photocatalysts based on graphitic carbon nitride. *Advanced Materials*, 27(13), 2150-2176.

[4] Wen, J., Xie, J., Chen, X., & Li, X. (2017). A review on g-C_3N_4-based photocatalysts. *Applied Surface Science*, *391*, 72-123.

[5] Hou, H., & Zhang, X. (2020). Rational design of 1D/2D heterostructured photocatalyst for energy and environmental applications. *Chemical Engineering Journal*, *395*, 125030.

[6] Yu, H., Jiang, L., Wang, H., Huang, B., Yuan, X., Huang, J., & Zeng, G. (2019). Modulation of Bi2MoO6-based materials for photocatalytic water splitting and environmental application: a critical review. *Small*, *15*(23), 1901008.

[7] Cheng, L., Xiang, Q., Liao, Y., & Zhang, H. (2018). CdS-based photocatalysts. *Energy & Environmental Science*, *11*(6), 1362-1391.

[8] Zhao, Z., Sun, Y., & Dong, F. (2015). Graphitic carbon nitride based nanocomposites: a review. *Nanoscale*, *7*(1), 15-37.

[9] Wang, Y., Wang, Q., Zhan, X., Wang, F., Safdar, M., & He, J. (2013). Visible light driven type II heterostructures and their enhanced photocatalysis properties: a review. *Nanoscale*, *5*(18), 8326-8339.

[10] Masih, D., Ma, Y., & Rohani, S. (2017). Graphitic C3N4 based noble-metal-free photocatalyst systems: a review. *Applied Catalysis B: Environmental*, *206*, 556-588.

[11] Xu, C., Anusuyadevi, P. R., Aymonier, C., Luque, R., & Marre, S. (2019). Nanostructured materials for photocatalysis. *Chemical Society Reviews*, *48*(14), 3868-3902.

[12] Xie, S., Wang, Z., Cheng, F., Zhang, P., Mai, W., & Tong, Y. (2017). Ceria and ceria-based nanostructured materials for photoenergy applications. *Nano Energy*, *34*, 313-337.

[13] De Pasquale, I., Lo Porto, C., Dell'Edera, M., Petronella, F., Agostiano, A., Curri, M. L., & Comparelli, R. (2020). Photocatalytic TiO2-Based Nanostructured Materials for Microbial Inactivation. *Catalysts*, *10*(12), 1382..

[14] Zhang, N., Wang, L., Wang, H., Cao, R., Wang, J., Bai, F., & Fan, H. (2018). Self-assembled one-dimensional porphyrin nanostructures with enhanced photocatalytic hydrogen generation. *Nano letters*, *18*(1), 560-566.

[15] Yuan, X., Floresyona, D., Aubert, P. H., Bui, T. T., Remita, S., Ghosh, S., & Remita, H. (2019). Photocatalytic degradation of organic pollutant with polypyrrole nanostructures under UV and visible light. *Applied Catalysis B: Environmental*, *242*, 284-292.

[16] Sonawane, R. S., Kale, B. B., & Dongare, M. K. (2004). Preparation and photo-catalytic activity of Fe-TiO2 thin films prepared by sol–gel dip coating. *Materials Chemistry and Physics*, 85(1), 52-57.

[17] Kumar, A., & Jain, A. K. (2001). Photophysics and photochemistry of colloidal CdS–TiO2 coupled semiconductors—photocatalytic oxidation of indole. *Journal of Molecular Catalysis A: Chemical*, 165(1-2), 265-273.

[18] Janitabar-Darzi, S., & Mahjoub, A. R. (2009). Investigation of phase transformations and photocatalytic properties of sol–gel prepared nanostructured ZnO/TiO2 composites. *Journal of Alloys and Compounds*, 486(1-2), 805-808.

[19] Tian, J., Chen, L., Yin, Y., Wang, X., Dai, J., Zhu, Z., ... & Wu, P. (2009). Photocatalyst of TiO2/ZnO nano composite film: preparation, characterization, and photodegradation activity of methyl orange. *Surface and Coatings Technology*, 204(1-2), 205-214.

[20] Baradaran, M., Ghodsi, F. E., Bittencourt, C., & Llobet, E. (2019). The role of Al concentration on improving the photocatalytic performance of nanostructured

ZnO/ZnO: Al/ZnO multilayer thin films. *Journal of Alloys and Compounds*, *788*, 289-301.

[21] Chappel, S., Chen, S. G., & Zaban, A. (2002). TiO2-coated nanoporous SnO2 electrodes for dye-sensitized solar cells. *Langmuir*, 18(8), 3336-3342.

[22] Wang, J. J., Wang, D. S., Wang, J., Zhao, W. L., & Wang, C. W. (2011). High transmittance and superhydrophilicity of porous TiO2/SiO2 bi-layer films without UV irradiation. *Surface and Coatings Technology*, 205(12), 3596-3599.

[23] Yosefi, L., & Haghighi, M. (2018). Fabrication of nanostructured flowerlike p-BiOI/p-NiO heterostructure and its efficient photocatalytic performance in water treatment under visible-light irradiation. *Applied Catalysis B: Environmental*, *220*, 367-378.

[24] Irie, H., Mori, H., & Hashimoto, K. (2004). Interfacial structure dependence of layered TiO2/WO3 thin films on the photoinduced hydrophilic property. *Vacuum*, 74(3-4), 625-629.

[25] Jiang, X., & Chen, X. (2004). Crystallization behavior and hydrophilic performances of V2O5–TiO2 films prepared by sol–gel dip-coating. *Journal of crystal growth*, 270(3-4), 547-552.

[26] Reddy, B. M., Ganesh, I., Reddy, E. P., Fernández, A., & Smirniotis, P. G. (2001). Surface characterization of Ga2O3− TiO2 and V2O5/Ga2O3− TiO2 catalysts. *The Journal of Physical Chemistry B*, 105(26), 6227-6235.

[27] Mao, L., Jiang, W., He, L., & Fang, P. (2011). Photocatalytic activity of TiO 2 sensitized by CdS quantum dots under visible-light irradiation. *Wuhan University Journal of Natural Sciences*, 16(4), 313.

[28] Qian, S., Wang, C., Liu, W., Zhu, Y., Yao, W., & Lu, X. (2011). An enhanced CdS/TiO2 photocatalyst with high stability and activity: effect of mesoporous substrate and bifunctional linking molecule. *Journal of Materials Chemistry*, 21(13), 4945-4952.

[29] Li, Y. S., Jiang, F. L., Xiao, Q., Li, R., Li, K., Zhang, M. F., ... & Liu, Y. (2010). Enhanced photocatalytic activities of TiO2 nanocomposites doped with water-soluble mercapto-capped CdTe quantum dots. *Applied Catalysis B: Environmental*, 101(1-2), 118-129.

[30] Fu, G., Vary, P. S., & Lin, C. T. (2005). Anatase TiO2 nanocomposites for antimicrobial coatings. *The journal of physical chemistry B*, 109(18), 8889-8898.

[31] Sun, W. T., Yu, Y., Pan, H. Y., Gao, X. F., Chen, Q., & Peng, L. M. (2008). CdS quantum dots sensitized TiO2 nanotube-array photoelectrodes. *Journal of the American Chemical Society*, 130(4), 1124-1125.

[32] Asahi, R. Y. O. J. I., Morikawa, T. A. K. E. S. H. I., Ohwaki, T., Aoki, K., & Taga, Y. (2001). Visible-light photocatalysis in nitrogen-doped titanium oxides. *science*, 293(5528), 269-271.

[33] Zhang, H., Lv, X., Li, Y., Wang, Y., & Li, J. (2010). P25-graphene composite as a high performance photocatalyst. *ACS nano*, 4(1), 380-386.

[34] Choi, W. (1994). Termin A. Hoffmamm M R. The role of metal ion dopants in quantumsized TiO: *I correlation between photoreactivity and charge carrier recombination dynamics*, 98(51), 13669-13679.

[35] Zaleska, A., Grabowska, E., Sobczak, J. W., Gazda, M., & Hupka, J. (2009). Photocatalytic activity of boron-modified TiO2 under visible light: The effect of boron content, calcination temperature and TiO2 matrix. *Applied Catalysis B: Environmenta*l, 89(3-4), 469-475.

[36] Dasgupta, N. P., Sun, J., Liu, C., Brittman, S., Andrews, S. C., Lim, J., & Yang, P. (2014). 25th anniversary article: semiconductor nanowires-synthesis, characterization, and applications. *Advanced materials*, 26(14), 2137-2184.

[37] Qin, L., Wang, G., & Tan, Y. (2018). Plasmonic Pt nanoparticles—TiO 2 hierarchical nano-architecture as a visible light photocatalyst for water splitting. *Scientific reports*, 8(1), 1-13.

[38] Sauvage, F. D. F. F. L. B. A., Di Fonzo, F., Li Bassi, A., Casari, C. S., Russo, V., Divitini, G., & Graetzel, M. (2010). Hierarchical TiO2 photoanode for dye-sensitized solar cells. *Nano letters*, 10(7), 2562-2567.

[39] Liao, J. Y., Lei, B. X., Chen, H. Y., Kuang, D. B., & Su, C. Y. (2012). Oriented hierarchical single crystalline anatase TiO 2 nanowire arrays on Ti-foil substrate for efficient flexible dye-sensitized solar cells. *Energy & Environmental Science*, 5(2), 5750-5757.

[40] Kim, H., & Yong, K. (2013). A highly efficient light capturing 2D (nanosheet)-1D (nanorod) combined hierarchical ZnO nanostructure for efficient quantum dot sensitized solar cells. *Physical Chemistry Chemical Physics*, 15(6), 2109-2116.

[41] Shao, F., Sun, J., Gao, L., Yang, S., & Luo, J. (2012). Forest-like TiO2 hierarchical structures for efficient dye-sensitized solar cells. *Journal of Materials Chemistry*, 22(14), 6824-6830.

[42] Wu, W. Q., Lei, B. X., Rao, H. S., Xu, Y. F., Wang, Y. F., Su, C. Y., & Kuang, D. B. (2013). Hydrothermal fabrication of hierarchically anatase TiO 2 nanowire arrays on FTO glass for dye-sensitized solar cells. *Scientific reports*, 3(1), 1-7.

[43] Cheng, C., & Fan, H. J. (2012). Branched nanowires: synthesis and energy applications. *Nano Today*, 7(4), 327-343.

[44] Roh, D. K., Chi, W. S., Jeon, H., Kim, S. J., & Kim, J. H. (2014). High efficiency solid-state dye-sensitized solar cells assembled with hierarchical anatase pine tree-like TiO2 nanotubes. *Advanced Functional Materials*, 24(3), 379-386.

[45] Wu, W. Q., Rao, H. S., Feng, H. L., Chen, H. Y., Kuang, D. B., & Su, C. Y. (2014). A family of vertically aligned nanowires with smooth, hierarchical and hyperbranched architectures for efficient energy conversion. *Nano Energy*, 9, 15-24.

[46] Fang, L., Chen, J., Zhang, M., Jiang, X., & Sun, Z. (2019). Introduction of Ti3+ ions into heterostructured TiO2 nanotree arrays for enhanced photoelectrochemical performance. *Applied Surface Science*, 490, 1-6.

[47] Miquelot, A., Debieu, O., Rouessac, V., Villeneuve, C., Prud'Homme, N., Cure, J., & Vahlas, C. (2019). TiO2 nanotree films for the production of green H2 by solar water splitting: From microstructural and optical characteristics to the photocatalytic properties. *Applied Surface Science*, 494, 1127-1137.

[48] Shimizu, K. I., Kaneko, T., Fujishima, T., Kodama, T., Yoshida, H., & Kitayama, Y. (2002). Selective oxidation of liquid hydrocarbons over photoirradiated TiO2 pillared clays. *Applied Catalysis A: General*, 225(1-2), 185-191.

[49] Shiraishi, Y., Saito, N., & Hirai, T. (2005). Adsorption-driven photocatalytic activity of mesoporous titanium dioxide. *Journal of the American Chemical Society*, 127(37), 12820-12822.

[50] Lang, X., Ma, W., Zhao, Y., Chen, C., Ji, H., & Zhao, J. (2012). Visible-Light-Induced Selective Photocatalytic Aerobic Oxidation of Amines into Imines on TiO2. *Chemistry-A European Journal*, 18(9), 2624-2631.

[51] Pillai, U. R., & Sahle-Demessie, E. (2002). Selective oxidation of alcohols in gas phase using light-activated titanium dioxide. *Journal of Catalysis*, 211(2), 434-444.

[52] Zhang, Y., Tang, Z. R., Fu, X., & Xu, Y. J. (2010). TiO2− graphene nanocomposites for gas-phase photocatalytic degradation of volatile aromatic pollutant: is TiO2− graphene truly different from other TiO2− carbon composite materials?. *ACS nano*, 4(12), 7303-7314.

[53] Tsukamoto, D., Shiraishi, Y., Sugano, Y., Ichikawa, S., Tanaka, S., & Hirai, T. (2012). Gold nanoparticles located at the interface of anatase/rutile TiO2 particles as active plasmonic photocatalysts for aerobic oxidation. *Journal of the American Chemical Society*, 134(14), 6309-6315.

[54] Shayegan, Z., Lee, C. S., & Haghighat, F. (2018). TiO2 photocatalyst for removal of volatile organic compounds in gas phase-A review. *Chemical Engineering Journal,* 334, 2408-2439.

[55] Sudrajat, H., Babel, S., Thushari, I., & Laohhasurayotin, K. (2019). Stability of La dopants in NaTaO3 photocatalysts. *Journal of Alloys and Compounds*, *775*, 1277-1285.

[56] Higashimoto, S., Kitao, N., Yoshida, N., Sakura, T., Azuma, M., Ohue, H., & Sakata, Y. (2009). Selective photocatalytic oxidation of benzyl alcohol and its derivatives into corresponding aldehydes by molecular oxygen on titanium dioxide under visible light irradiation. *Journal of Catalysis*, 266(2), 279-285.

[57] Hoffmann, M. R., Martin, S. T., Choi, W., & Bahnemann, D. W. (1995). Environmental applications of semiconductor photocatalysis. *Chemical reviews*, 95(1), 69-96.

[58] Hu, C. C., Huang, H. H., & Huang, Y. C. (2017). N-doped NaTaO3 synthesized from a hydrothermal method for photocatalytic water splitting under visible light irradiation. *Journal of energy chemistry*, *26*(3), 515-521.

[59] Kitano, S., Tanaka, A., Hashimoto, K., & Kominami, H. (2014). Selective oxidation of alcohols in aqueous suspensions of rhodium ion-modified TiO 2 photocatalysts under irradiation of visible light. *Physical Chemistry Chemical Physics*, 16(24), 12554-12559.

[60] Higashimoto, S., Shirai, R., Osano, Y., Azuma, M., Ohue, H., Sakata, Y., & Kobayashi, H. (2014). Influence of metal ions on the photocatalytic activity: Selective oxidation of benzyl alcohol on iron (III) ion-modified TiO2 using visible light. *Journal of catalysis*, 311, 137-143.

[61] Tamiolakis, I., Lykakis, I. N., & Armatas, G. S. (2015). Mesoporous CdS-sensitized TiO2 nanoparticle assemblies with enhanced photocatalytic properties: selective aerobic oxidation of benzyl alcohols. *Catalysis Today*, 250, 180-186.

[62] Chen, Y., Wang, Y., Li, W., Yang, Q., Hou, Q., Wei, L., & Ju, M. (2017). Enhancement of photocatalytic performance with the use of noble-metal-decorated TiO2 nanocrystals as highly active catalysts for aerobic oxidation under visible-light irradiation. *Applied Catalysis B: Environmental*, 210, 352-367.

[63] Zhang, L., Liu, D., Guan, J., Chen, X., Guo, X., Zhao, F., & Mu, X. (2014). Metal-free g-C3N4 photocatalyst by sulfuric acid activation for selective aerobic oxidation of benzyl alcohol under visible light. *Materials Research Bulletin*, 59, 84-92.

[64] Shen, S., Guo, P., Zhao, L., Du, Y., & Guo, L. (2011). Insights into photoluminescence property and photocatalytic activity of cubic and rhombohedral ZnIn2S4. *Journal of Solid State Chemistry*, *184*(8), 2250-2256.

[65] Dai, X., Xie, M., Meng, S., Fu, X., & Chen, S. (2014). Coupled systems for selective oxidation of aromatic alcohols to aldehydes and reduction of nitrobenzene into aniline using CdS/g-C3N4 photocatalyst under visible light irradiation. *Applied Catalysis B: Environmental*, 158, 382-390.

[66] Liang, Z., Yan, C. F., Rtimi, S., & Bandara, J. (2019). Piezoelectric materials for catalytic/photocatalytic removal of pollutants: Recent advances and outlook. *Applied Catalysis B: Environmental*, *241*, 256-269.

[67] Dong, H., Guo, X., Yang, C., & Ouyang, Z. (2018). Synthesis of g-C3N4 by different precursors under burning explosion effect and its photocatalytic degradation for tylosin. *Applied Catalysis B: Environmental*, *230*, 65-76.

[68] Long, J., Wang, S., Ding, Z., Wang, S., Zhou, Y., Huang, L., & Wang, X. (2012). Amine-functionalized zirconium metal-organic framework as efficient visible-light photocatalyst for aerobic organic transformations. *Chemical Communications*, 48(95), 11656-11658.

[69] Song, L. N., Ding, F., Yang, Y. K., Ding, D., Chen, L., Au, C. T., & Yin, S. F. (2018). Synthesis of TiO2/Bi2MoO6 composite for partial oxidation of aromatic alkanes under visible-light illumination. *ACS Sustainable Chemistry & Engineering*, 6(12), 17044-17050.

[70] Liu, Q., Wang, M., He, Y., Wang, X., & Su, W. (2018). Photochemical route for synthesizing Co-P alloy decorated ZnIn 2 S 4 with enhanced photocatalytic H 2 production activity under visible light irradiation. *Nanoscale*, 10(40), 19100-19106.

[71] Yu, J., Li, J., Wei, H., Zheng, J., Su, H., & Wang, X. (2014). Hydrotalcite-supported gold catalysts for a selective aerobic oxidation of benzyl alcohol driven by visible light. *Journal of Molecular Catalysis A: Chemical*, 395, 128-136.

[72] Li, B., Shao, L., Wang, R., Dong, X., Zhao, F., Gao, P., & Li, Z. (2018). Interfacial synergism of Pd-decorated BiOCl ultrathin nanosheets for the selective oxidation of aromatic alcohols. *Journal of Materials Chemistry A*, 6(15), 6344-6355.

[73] Christopher, P., Xin, H., Marimuthu, A., & Linic, S. (2012). Singular characteristics and unique chemical bond activation mechanisms of photocatalytic reactions on plasmonic nanostructures. *Nature materials*, 11(12), 1044-1050.

[74] Qiu, P., Yao, J., Chen, H., Jiang, F., & Xie, X. (2016). Enhanced visible-light photocatalytic decomposition of 2, 4-dichlorophenoxyacetic acid over ZnIn2S4/g-C3N4 photocatalyst. *Journal of hazardous materials*, 317, 158-168.

[75] Wang, H., Yuan, X., Wang, H., Chen, X., Wu, Z., Jiang, L., & Zeng, G. (2016). Facile synthesis of Sb2S3/ultrathin g-C3N4 sheets heterostructures embedded with g-C3N4 quantum dots with enhanced NIR-light photocatalytic performance. *Applied Catalysis B: Environmental*, 193, 36-46.

[76] Kolny-Olesiak, J., & Weller, H. (2013). Synthesis and application of colloidal CuInS2 semiconductor nanocrystals. *ACS applied materials & interfaces*, 5(23), 12221-12237.

[77] Bai, X., & Li, J. (2011). Photocatalytic hydrogen generation over porous ZnIn2S4 microspheres synthesized via a CPBr-assisted hydrothermal method. *Materials Research Bulletin*, 46(7), 1028-1034.

[78] Sriram, M. A., McMichael, P. H., Waghray, A., Kumta, P. N., Misture, S., & Wang, X. L. (1998). Chemical synthesis of the high-pressure cubic-spinel phase of ZnIn2S4. *Journal of materials science*, 33(17), 4333-4339.

[79] Shen, J., Zai, J., Yuan, Y., & Qian, X. (2012). 3D hierarchical ZnIn2S4: the preparation and photocatalytic properties on water splitting. *International journal of hydrogen energy*, 37(22), 16986-16993.

[80] Lei, Z., You, W., Liu, M., Zhou, G., Takata, T., Hara, M., & Li, C. (2003). Photocatalytic water reduction under visible light on a novel ZnIn 2 S 4 catalyst synthesized by hydrothermal method. *Chemical Communications*, (17), 2142-2143.

[81] Chai B, Peng T,Zeng P, et al. Template-free hydrothermal synthesis of ZnInpS4 floriatedmicrosphere as an efficient photocatalyst for H production under visible-light irradiation[J].*Journal ofPhysical Chemistry c*, 2011,115(13): 6149-6155.

[82] Shi, L., Yin, P., & Dai, Y. (2013). Synthesis and photocatalytic performance of ZnIn2S4 nanotubes and nanowires. *Langmuir*, 29(41), 12818-12822.

[83] Shen, S., Zhao, L., Zhou, Z., & Guo, L. (2008). Enhanced photocatalytic hydrogen evolution over Cu-doped ZnIn2S4 under visible light irradiation. *The Journal of Physical Chemistry C*, 112(41), 16148-16155.

[84] Chen, J., Xin, F., Yin, X., Xiang, T., & Wang, Y. (2015). Synthesis of hexagonal and cubic ZnIn 2 S 4 nanosheets for the photocatalytic reduction of CO 2 with methanol. *RSC Advances*, 5(5), 3833-3839.

[85] Jiang, R., Li, B., Fang, C., & Wang, J. (2014). Metal/semiconductor hybrid nanostructures for plasmon-enhanced applications. *Advanced materials*, 26(31), 5274-5309.

[86] Chen, Y., Hu, S., Liu, W., Chen, X., Wu, L., Wang, X., & Li, Z. (2011). Controlled syntheses of cubic and hexagonal ZnIn 2 S 4 nanostructures with different visible-light photocatalytic performance. *Dalton Transactions*, 40(11), 2607-2613.

[87] Shen, S., Zhao, L., & Guo, L. (2008). Morphology, structure and photocatalytic performance of ZnIn2S4 synthesized via a solvothermal/hydrothermal route in different solvents. *Journal of Physics and chemistry of Solids*, 69(10), 2426-2432.

[88] Ebadi, M., Ramezani, M., & Zarghami, Z. (2016). A Facile Hydrothermal Route to the Synthesis of ZnIn 2 S 4 Quantum Dots in the Presence of Thioglycolic Acid and Investigation Its Light Harvesting Application. *Journal of Cluster Science*, 27(1), 341-350.

[89] Shen, S., Zhao, L., & Guo, L. (2009). Crystallite, optical and photocatalytic properties of visible-light-driven ZnIn2S4 photocatalysts synthesized via a surfactant-assisted hydrothermal method. *Materials Research Bulletin*, 44(1), 100-105.

[90] Hu, X., Yu, J. C., Gong, J., & Li, Q. (2007). Rapid mass production of hierarchically porous ZnIn2S4 submicrospheres via a microwave-solvothermal process. *Crystal Growth and Design*, 7(12), 2444-2448.

[91] Carević, M. V., Savić, T. D., Abazović, N. D., Mitrić, M. N., Stojanović, Z. A., Ahrenkiel, S. P., & Čomor, M. I. (2017). Formation of ZnIn2S4 nanosheets and tubular structures in organic media. *Materials Research Bulletin*, 87, 140-147.

[92] Liu, H., Jin, Z., Xu, Z., Zhang, Z., & Ao, D. (2015). Fabrication of ZnIn2S4–gC3N4 sheet-on-sheet nanocomposites for efficient visible-light photocatalytic H 2-evolution and degradation of organic pollutants. *RSC Advances*, *5*(119), 97951-97961.

[93] Christoforidis, K. C., Montini, T., Bontempi, E., Zafeiratos, S., Jaén, J. J. D., & Fornasiero, P. (2016). Synthesis and photocatalytic application of visible-light active β-Fe2O3/g-C3N4 hybrid nanocomposites. *Applied Catalysis B: Environmental*, 187, 171-180.

[94] Kumar, S., Surendar, T., Baruah, A., & Shanker, V. (2013). Synthesis of a novel and stable g-C3N4–Ag3PO4 hybrid nanocomposite photocatalyst and study of the photocatalytic activity under visible light irradiation. *Journal of Materials Chemistry A*, 1(17), 5333-5340.

[95] Pan, C., & Zhu, Y. (2010). New type of BiPO4 oxy-acid salt photocatalyst with high photocatalytic activity on degradation of dye. *Environmental science & technology*, 44(14), 5570-5574.

[96] Yang, Y., Guo, Y., Liu, F., Yuan, X., Guo, Y., Zhang, S., & Huo, M. (2013). Preparation and enhanced visible-light photocatalytic activity of silver deposited graphitic carbon nitride plasmonic photocatalyst. *Applied Catalysis B: Environmental*, 142, 828-837.

[97] Qin, W., Zhang, D., Zhao, D., Wang, L., & Zheng, K. (2010). Near-infrared photocatalysis based on YF3: Yb3+, Tm3+/TiO2 core/shell nanoparticles. *Chemical communications*, 46(13), 2304-2306.

[98] Meng, F., Luo, Y., Zhou, Y., Zhang, J., Zheng, Y., Cao, G., & Tao, X. (2016). Integrated plasmonic and upconversion starlike Y2O3: Er/Au@ TiO2 composite for enhanced photon harvesting in dye-sensitized solar cells. *Journal of Power Sources*, 316, 207-214.

[99] Liu, X., Dong, G., Li, S., Lu, G., & Bi, Y. (2016). Direct observation of charge separation on anatase TiO2 crystals with selectively etched {001} facets. *Journal of the American Chemical Society*, 138(9), 2917-2920.